

A simulation framework for predicting process-induced distortions for precise manufacturing of aerospace thermoset composites.

Neoklis Traiforos^{a,c}, Thomas Turner^c, Patrik Runeberg^b, Daoud Fernass^a,
Dimitrios Chronopoulos^c, Florian Glock^a, Gerd Schuhmacher^a, Daniel
Hartung^b

^a*Airbus Defence and Space GmbH, Rechliner Str., 85077, Manching, Germany*

^b*Premium AEROTECH GmbH, Hawnstetter Str. 225, 86179, Augsburg, Germany*

^c*The University of Nottingham, Faculty of Engineering, Polymer Composites Research Group, Advanced Manufacturing Building, 522 Derby Rd, Nottingham NG8 1BB, United Kingdom*

Abstract

The choice of a suitable material model to simulate process induced distortions is important in order to achieve a right first time approach in the design of new moulds. This work investigates the ability of the Cure Hardening Instantaneously Linear Elastic (CHILE) model and a linear viscoelastic material model to predict process induced distortions of an aerospace composite frame. The material models were coupled with a cure kinetics model and a chemical shrinkage model in order to capture the multi-physics phenomena that take place during the curing process. The modelling of the viscoelastic behaviour of the resin is performed with the use of a generalized Maxwell model. A novel methodology is applied for shifting the relaxation times of the composite based on its temperature and degree of cure. It is shown that the viscoelastic model more accurately predicts the measured distortions due to its ability to account for stress relaxation.

Keywords:

Process induced distortions, Thermoset composite materials, Finite element analysis (FEA), Aerospace structures, Process simulation, Dimensional control

1. Introduction

A goal in the manufacturing industry is to achieve a right first time approach. The application of this principle in the design process of moulds for composites parts leads to significant reductions in the lead times and manufacturing costs. This is achieved by reducing the number of tools that have to be manufactured or modified until a tool geometry is certified to produce the part of the required quality.

Process Induced Distortions (PID) are inevitably present in composite structures manufacturing. They are defined as the deviation of the structure from its nominal CAD geometry and are the combined effect of spring-in and warpage, which are the two deformation mechanisms that coexist in complex composite structures to some degree [1]. The residual stresses which are imposed on the part from its manufacturing process and are responsible for its deformation field, are usually not known a priori to the designer of the mould. Thus, an iterative mould design process is employed, which includes the manufacturing of the mould, measuring the distortions of the part and re-machining the mould geometry accordingly in order to reduce the distortions of the part.

To achieve a right first time approach, the designer should be able to make an accurate estimation of the distortions that are imposed on the composite structure from its manufacturing process. This knowledge will enable the designer to compensate for the distortions of the part by adjusting the tool geometry [2]. This design approach known as mould geometry compensation is widely employed by the aerospace industry (Fig. B.1), as it minimises the loads that have to be applied to assemble the structure and the use of shims which increase the weight of the assembly [3]. However, in complex geometries like the composite frame studied here, an accurate estimation of process induced distortions is an open research topic [4, 5, 6, 7]. This is due to the variety of factors that contribute to process induced distortions and due to the fact that in industrial applications a generally applicable, robust, fast yet accurate simulation process is sought.

1.1. Factors that affect PID

Various researchers have investigated both experimentally [8] and numerically the factors which create residual stresses in the composite structures that lead to shape distortions [9, 10, 11].

Svanberg in his research tried to evaluate and separate the factors that contribute to shape distortions into four main categories according to their relative significance [12]. The difference in the Coefficient of Thermal Expansion (CTE) between the matrix and the fibres, the chemical shrinkage of the resin, the laminate lay-up as well as the CTE of the mould are reported to have a large effect on the induced residual stresses in the part. The void content and the fibre content gradients of the composite have moderate effect. On the other hand, cure time and mould thermal conductivity are reported by Svanberg to have small or no effect at all on shape distortions.

C. Albert et al. were the first to separate the factors that affect shape distortions into two different categories namely intrinsic and extrinsic [1]. Intrinsic parameters are defined as parameters related to part geometry and material properties. These parameters arise from inside the structure and are the result of the composites constituents (namely the matrix and the fibres). On the other hand, extrinsic parameters are defined as parameters related to tooling or processing and arise from the environmental conditions in which the structure is operating or from the manufacturing process of the structure (curing cycle, tool part interaction etc.).

The researchers experimentally investigated the individual and interactive effects of five design parameters: part shape, layup, flange length, part thickness, and part angle, and three process parameters: tool material, tool surface and cure cycle, on spring-in and warpage of C- and L-shaped composite specimens [1]. They concluded that both design and process parameters can have a significant effect on spring-in and warpage and that there are multiple interactions between them. The researchers also found that aluminium tooling always gives more spring-in than steel tooling, a statement also confirmed by Kappel [13]. By studying tool-part interaction on C- and L-profile specimens Kappel concluded that it is driven by the difference between the CTE of the mould and the composite structure when this is pressed to the mould because of the autoclave pressure along with geometrical locking if this is present. Thus, a higher tool CTE leads to increasing web warpage and web warpage occurs even though a thermally compatible INVAR tooling is used [13]. Furthermore, Zeng et al. suggest that the shape of the part has significant influence on the warpage [14].

D. Stefaniak et al. [15] through their experimental investigations affirm that warpage deformation of symmetric and initially flat laminates is mainly driven by mechanical tool-part interaction as a non-uniform stress distribution field is locked in on the through thickness direction as the resin cures.

Furthermore, tool surface roughness is observed to influence the magnitude of these deformations significantly. The authors observed larger deflections for higher tool coarseness values when no release film is used. Furthermore, the use of release film on top of the tooling is able to transfer noticeable amounts of shear stress and affect the deformations. This is in agreement with the research of Liangliang et al. that the use of a PTFE release film cannot eliminate the effect of the tool-part interaction [16]. However, the magnitude of the effect of the release film on the warpage of the part depend on the resin system used and on the coarseness of the tool surface.

N. Ersoy et al. investigated the development of spring-in angle during cure of AS4/8552 thermosetting composite C-shaped specimens by using a cure quench technique [17]. In their research they concluded that the thermoelastic component of spring-in, which refers to the shape change due to the mismatch of CTE in the in-plane and through-the-thickness directions, accounts for 50% of the final spring-in of fully cured components, while the non-thermoelastic component of the spring-in, which is predominantly due to cure shrinkage, accounts for the rest. They also concluded that for partially cured specimens, the reason cure shrinkage and thermal effects before vitrification contribute to spring-in is because they cause a geometrical change in shape, which does not require substantial stresses to sustain it. As a result they suggest that a postcuring operation will contribute to the reduction of the spring-in angles of partially cured parts.

In their effort to improve the accuracy of predictions of process-induced distortions after cool down of carbon-fiber-epoxy composite frames E. Kappel et al. studied the CTE of orthotropic laminates [18]. They found that measured CTEs increasingly deviate from theoretical CTE values, derived from unidirectional ply data using the CLT theory, when the degree of laminate orthotropy, which is quantified by the in-plane Youngs modulus ratio E_x/E_y , increases. They consider the observed effect as critical, as inhomogeneous CTEs lead to process-induced distortions of curved composite structures. Thus, they play a key role when carbon-fiber-epoxy composite frames shall be made in tight dimensional tolerances. Wrong CTE calculation leads to erroneous shape predictions, inaccurate tool compensation and finally to assembly problems. Furthermore, to reduce the mismatch of resin contraction and fiber contraction during the cure stage Hsiao et al. proposed to infuse a small amount of carbon nanofibers (CNFs) into the preform while manufacturing composite parts with the use of vacuum assisted resin transfer moulding (VARTM) process [19].

Process induced distortions of T-stiffeners and sandwich structures have also been investigated with the intention of increasing dimensional control of aerospace structures [20]. It was found that by increasing sandwich core thickness the spring-in behaviour declines [21] while Mahadik et al. found that the thermal expansion and Poissons ratio of the foam core were the major contributors to spring-in [22].

1.2. Simulation approaches and material models

Analytical [23, 24, 25, 26, 27], semi analytical [28, 29] and numerical approaches have been proposed to calculate process induced distortions [30, 31].

The analytical models offer fast calculation times and are used within the academia to validate new numerical models as well as by industry to get a first estimation of the expected spring-in angle of the structure. However, since their development is based on flat or C- and L-profile specimens they are not considered suitable for an accurate prediction of process induced distortions of complex geometries. Semi analytical models require as input experimentally derived values of the studied structure and are able to take into account factors (eg thickness of the structure) that pure analytical models cannot.

A complete numerical process to simulate process induced distortions contains a fiber compaction simulation in order to ensure that no (or minimum) fiber wrinkling, bridging and fiber reorientation exist on the preform followed by a resin flow simulation to calculate the distribution of fiber volume fraction in the part.

Hubert [32] studied flow and compaction modelling on angled composite laminates. Lightfoot et al. [33] studied the mechanisms responsible for fiber wrinkling and fiber misalignment of unidirectional plies during layup of prepreg in the tool while Potter et al. [34] directly measured fiber misalignment in as-delivered prepreps and observed that the material had fiber waviness. Furthermore, Lamers [35] studied and modelled shape distortions of composite structures due to processing induced fiber reorientation.

Then a sequentially coupled or fully coupled thermal-chemical-analysis will enable the calculation of temperature and degree of cure distribution in the part. The mapping of these fields to the mechanical analysis with the use of a material constitutive equation results in the calculation of the residuals stresses and the respective process induced distortions of the part [36, 37, 38].

However, a complete simulation process, as presented above, for the prediction of process induced distortions is rarely employed in the industry for every part as it would require extensive material characterization, expertise and processing power. Usually, assumptions are made like a uniform fiber volume fraction and temperature field in the part omitting much of the multi-physics complexity.

To employ numerical approaches to calculate process-induced distortions various material models have been proposed. Elastic material models make use of the Hooke's law constitutive equation, and assume that the residual stresses in the structure are starting to build up after the part has been cured and starts to cool down to room temperature from its final hold temperature.

However, Ding et al. concluded in their research that pure elastic models can provide a good prediction of residual stress only for thin laminates [39]. This is because of the complex temperature field gradients in thick laminates and resulting inhomogeneous through-thickness degree of cure evolution [40]. Moreover, elastic models omit the effects of chemical shrinkage, the development of residual stress before cool-down and stress relaxation during the cure and cool down process [41]. To account for some of these deficiencies Bogetti et al. studied residual stresses and deformation of thick composite laminates and proposed a simulation process able to take into account the chemical shrinkage of the resin during cure [42].

Moreover, Andrew A. Johnston proposed the Cure Hardening Instantaneously Linear Elastic (CHILE) constitutive model [43]. According to this material model the evolution of the resin modulus can be divided into three stages during the cure with that being the viscous state, the state where the modulus quickly builds up and the fully cured state where no chemical reaction takes place. With the use of the CHILE material model the chemical shrinkage of the matrix can be taken into account. With the use of the CHILE material model Guiming Zhang et al. performed computational research on process-induced deformation of L-shaped variable-stiffness composite structures during cure and investigated the influence of corner radius, laminate thickness and flange length on spring-in [44].

The CHILE model however, is still instantaneously elastic model and cannot predict the stresses relaxation during curing, cool down or post curing, as it is not a time dependent model [41] [40]. In order to incorporate all the time dependent factors that affect shape distortions during the manufacturing process of thermoset composites, like heating and cooling rates, stress relaxation and cure time, viscoelastic material models are needed.

According to Zhang et al. an accurate simulation on the cure-induced residual stress should include the least two states of the entire cure process (relaxed state, a viscoelastic state and an elastic state), and consider the stress relaxation, thermal deformation and chemical shrinkage of the composite [41]. Furthermore, Benavente with the use of a viscoelastic material model predicted significant geometrical distortions at temperatures below the glass transition temperature which were not possible to predict with the use of elastic or CHILE model [36].

However, the viscoelastic material models have complex numerical model formulations compared to elastic or the CHILE model. Furthermore, viscoelastic material models require longer calculation times and large amount of memory to run because of the need to store model state variables from the previous time step to calculate the stresses at the current time step. Moreover, extensive material characterization is needed in order to derive the necessary viscoelastic material properties for the viscoelastic models to run.

Zocher et al. [45] presented a novel finite element scheme for linear anisotropic viscoelasticity. The authors introduced a smart integration point constitutive update algorithm whereby the stress increment is separated into a part which is linear in the strain increment, and a non-linear contribution which can be computed from stored results in the previous increment. However, they make the assumption of a single reduced time for all directions which may be physically unrealistic for materials, such as fibre-reinforced composites.

Harrison Poon and M. Fouad Ahmad proposed a constitutive update scheme for simulating anisotropic, thermo rheologically simple, viscoelastic solids [46] very similar in spirit to Zocher et al. With proper choice of state variables their model obviates the need for non-physical assumptions such as linear time variation of strain throughout the increment an assumptions which is adopted by Zocher et al [45]. The model takes as input the converged values of stress, strain and state variables at time n and the estimated strain at time $n + 1$ and updates the stress tensor, state variables and the Consistent Tangent Operator (CTO), which is used in a Newton type iterative scheme. Harrison Poon and M. Fouad Ahmad in a later publication extended their linear viscoelastic model to simulate solids exhibiting non-linearity of the Schapery type [47, 48]. This model is more appropriate to simulate cases where large deformations are expected and in cases where the material changes its properties under deformation.

Eom et al. [49] have proposed a phenomenological model for the calculation of the relaxation modulus of a thermosetting system over the complete range of cure. O'Brien et al. [50] experimentally investigated the cure dependent relaxation modulus of an epoxy system over the entire range of cure extent and used the acquired data to develop a practical model for predicting the cure dependence of the relaxation modulus throughout cure under varying processing conditions. However, both approaches require extensive material characterization over the entire cure range.

Finally, Ding et al. developed a three dimensional viscoelastic material model to simulate thermo-rheologically simple materials and extended their model to simulate also thermo-rheologically complex materials [39, 40]. In thermo-rheologically simple materials (TSMs) the unrelaxed stiffness (the stiffness in the glassy state) and the equilibrium stiffness (the stiffness in the rubbery state) are temperature and degree of cure independent. On the other hand on thermo-rheologically complex materials (TCMs) the equilibrium stiffness is temperature dependent. However, the description of thermo-rheologically complex materials requires the most extensive material characterisation and is considered to be cost prohibitive for most industrial purposes.

1.3. Scope of the research

The scope of this research is to investigate a simulation framework suitable for the simulation of process induced distortions of large aerospace composite frames. Since stress relaxation is reported by various researchers as an important factor to be considered to accurately predict shape distortions of the studied part after demoulding [51, 52], the linear viscoelastic material model proposed by Harrison Poon [46] was chosen to be evaluated. This was done due to its simple mathematical formulation compared to the material models proposed by Ding et al [39, 40] and due to the convenient numerical implementation with the use of a commercial implicit finite element solver.

We hereby present for the first time the combination of the time-cure-temperature superposition principle originally presented by Simon et.al [53] with the linear viscoelastic material model proposed by Harrison Poon [46]. A novel feature in this research is the application of time-cure-temperature superposition principle with the use of the Williams-Landel-Ferry (WLF) model for both the temperature and degree of cure shift, instead of the use of the Arrhenius equation employed by Simon et.al, as the agreement of the material tested with the WLF formulation was very good.

As a reference for comparing the results of the viscoelastic material model the CHILE material model is used which is often employed in the industry due to its simplicity and fast calculation times. Both material models were coupled with a cure kinetics model, functions to calculate instantaneous fibre volume fraction and Poisson's coefficient of the composite material and use the same micromechanics model to calculate lamina properties.

The proposed simulation framework focuses on the material modelling of thin wall (5 mm approximately) structures from the gelation point of the structure (after the fabric compaction and resin infusion process have been completed) to consolidation and demolding by deliberately omitting much of the multi-physics complexity prior to that point. However, the extension of the proposed simulation frameworks to capture this increased complexity would not require changes to the proposed modelling approach but only the addition of the relevant functionalities.

While the majority of the numerical and experimental investigations on process induced distortions found in the literature focus on flat, C- and L-shaped composite specimens, in this research a complex composite frame from the door surround structure of A350 aircraft was studied. A comparison between the simulation results of the material models tested against 3D measurement data of the manufactured frame is presented here for the first time and the deformation modes that act on the frame are discussed.

The aim of this research is to contribute to the maturity and adoption of higher fidelity process induced distortions simulation frameworks by OEMs and suppliers in the manufacturing process of aerospace composite frames.

2. Material Modelling

Since fiber properties within a composite structure do not substantially change, the modelling effort focuses on the evolution of the resin properties during cure. A mechanical-chemical simulation approach was adopted where the material properties of the resin depend on the degree of cure of the resin at each time step. To reduce computational time and modelling complexity it was assumed that the laminate has a homogeneous temperature field at each time step. In other words no temperature gradients exist in the part at a given time.

The composite system studied in this paper is composed of IMS65 fibers (supplied by the Toho Tenax) and EPS600 resin (supplied by Hexion). An overview of the material modelling effort is depicted in Fig. B.2, where

the function for the calculation of the shift factor a_{Tx} is employed only by the viscoelastic material model. However, the proposed material modelling approach as depicted in Fig. B.2 is still applicable over a wide range of thermoset composite systems by the substitution of the specific material constants or models (cure kinetics model, CTE material constants etc.) with the respective material constants or models of the resin system of interest.

2.1. Cure kinetic model

The first step in the simulation of both material models is the calculation of the degree of cure. For the calculation of the degree of cure at each time step equation (1) was used, which is the result of the linear combination of two autocatalytic models as presented by Lee et al. [54] with one of them combined with a diffusion factor function as proposed by Cole et al. [55].

$$\dot{\alpha} = \frac{A_1 e^{-\frac{E_{a1}}{RT}} \alpha^{m_1} (1 - \alpha)^{n_1}}{1 + e^{C(\alpha - (\alpha_{c0} + \alpha_{cT} T))}} + A_2 e^{-\frac{E_{a2}}{RT}} \alpha^{m_2} (1 - \alpha)^{n_2} \quad (1)$$

where :

- $\dot{\alpha}$: Degree of cure rate
- R : Universal gas constant
- T : Temperature (K)
- A_1, A_2 : Arrhenius constants
- E_{a1}, E_{a2} : Activation energies of the autocatalytic models
- $m_1, n_1, C, \alpha_{c0}, \alpha_{cT}, m_2, n_2$: Material constants

In order to calculate the degree of cure α from the curing rate $\dot{\alpha}$ Simpson's integration is used.

Dynamic scanning calorimetry (DSC) was used to characterize the cure kinetics of the EPS600 resin system. The experimental investigations were carried out according to the ISO 11357 standard. Then Eq.(1) was fitted to the experimental data with the use of least-square fit and the material constants of the equation were determined. The maximum deviation of Eq.(1) from the experimental data is 2%.

2.2. Glass Transition Temperature

The calculation of the degree of cure α at each time step enables the calculation of the glass transition temperature T_g of the resin. This is done with the use of the DiBenedetto equation Eq.(2):

$$T_g = T_{g0} + \frac{\alpha\lambda(T_g^\infty - T_g^0)}{1 - (1 - \lambda)\alpha} \quad (2)$$

where :

- λ : DiBenedetto material constant
- α : Degree of cure
- T_g^0 : Glass transition temperature at α^0 ($\alpha = 0$)
- T_g^∞ : Glass transition temperature at α^∞ ($\alpha = 1$)

DSC was also used to measure the T_g of five resin specimens and determine the DiBenedetto material constant λ by least squares fit of Eq.(2) to the experimental results. The degree of cure of the manufactured specimens was $\alpha=0$, $\alpha=0.15$, $\alpha=0.25$, $\alpha=0.4$ and $\alpha=1$.

2.3. Coefficient of Thermal Expansion

The CTE of the EPS600 resin was measured with the use of DMA. Three specimens were manufactured from the same tool and measured from room temperature to $250^\circ C$. The CTE of the resin depends on the state of the resin during the curing cycle. In the rubbery state the CTE of the resin was approximated as 2.5 times greater than the CTE of the resin in the glassy state according to the assumption made by Svanberg [12]. Eq.(3) was used to determine the CTE according to its state [12]:

$$\alpha_r^{CTE} = \begin{cases} \alpha_{rub}^{CTE} & T_{C1} < T^* \\ C_2 + C_3T^* + C_4T^{*2} & T_{C2} < T^* < T_{C1} \\ \alpha_{glass}^{CTE} + \alpha_\alpha(T^* - T_{C2}) & T^* < T_{C2} \end{cases} \quad (3)$$

where :

$$T^* = T - T_g \quad (4)$$

The quantities α_{rub}^{CTE} and α_{glass}^{CTE} are the coefficient of thermal expansion of the resin at the rubbery and glassy state respectively. $T_{C1}, T_{C2}, C_2, C_3, C_4, \alpha_\alpha$ used in Eq.(3) are material constants. T is the resin temperature and T_g is the glass transition temperature. To determine these material constants Eq.(3) was fitted to the experimental measurements.

2.4. Volumetric chemical shrinkage of the resin

The volumetric chemical shrinkage of the resin could be experimentally measured from the gel point of the resin (Technical University of Munich, Chair of Carbon Composites). Four specimens were manufactured and measured with the use of a rheometer according to the ASTM D 4473 standard. Then the resin chemical contraction model Eq.(5) proposed by Johnston [43] based on the work of Bogetti [42] was fitted to the experimental measurements to describe the evolution of the resin's chemical shrinkage. The volumetric chemical shrinkage of the resin before the gelation point was approximated as zero.

$$\mathbf{V}_r^C = \begin{cases} 0.0 & \alpha < \alpha_{c1} \\ B\alpha_c + (\mathbf{V}_r^{C\infty} - B)\alpha_c^2 & \alpha_{c1} \leq \alpha < \alpha_{c2} \\ \mathbf{V}_r^{C\infty} & \alpha \geq \alpha_{c2} \end{cases} \quad (5)$$

where :

$$\alpha_c = \frac{\alpha - \alpha_{c1}}{\alpha_{c2} - \alpha_{c1}} \quad (6)$$

The quantities $B, \alpha_{c1}, \alpha_{c2}$ used in Eq.(5) are material constants, $\mathbf{V}_r^{C\infty}$ is the maximum volumetric chemical shrinkage of the resin and α is the degree of cure.

2.5. Resin thermal and chemical strain

2.5.1. Resin thermal strain:

The resin is assumed to be an isotropic material having the same CTE at its all principal directions. To calculate the resin linear expansional strains equation (7)is employed:

$$\boldsymbol{\varepsilon}_r^T = \boldsymbol{\alpha}_r^{CTE} \Delta T \quad (7)$$

where:

- α_r^{CTE} : Coefficient of thermal expansion of the resin
- ΔT : Increment of temperature

2.5.2. Resin chemical strain:

Similarly to the calculation of thermal strains, uniform strain contraction for all principal strain components is assumed. To calculate the isotropic chemical shrinkage strain, equation (8) was used [42]:

$$\epsilon_r^C = (1 + V_r^C)^{\frac{1}{3}} - 1.0 \quad (8)$$

where V_r^C is the instantaneous volumetric chemical shrinkage of the resin.

2.6. Lamina fiber volume fraction

As the resin changes its volume during the curing cycle due to chemical shrinkage and thermal expansion the fiber volume fraction of the laminate consequently evolves. In order to calculate the lamina's instantaneous fiber volume fraction the following calculation process is employed :

- Calculation of the resin's specific volume at final product Eq.(9):

$$V_r^{Final} = 1.0 - V_{void} - V_f^{Final} \quad (9)$$

where :

- V_r^{Final} : Specific volume of the resin in the final product
- V_{void} : Specific volume of the voids in the final product.
- V_f^{Final} : Fiber volume fraction of the final product.
- Calculation of the resin's specific volume at the start of the manufacturing process based on its value in the final product Eq.(10):

$$V_r^{Start} = \frac{V_r^{Final}}{1 - V_r^{C\infty}} \quad (10)$$

where:

- $V_r^{C\infty}$: Resin specific volume maximum chemical contraction. (material constant)

- Calculation of the resin's specific volume change due to thermal strains Eq.(11) [42]:

$$V_r^T = \varepsilon_{1T} + \varepsilon_{2T} + \varepsilon_{3T} + \varepsilon_{1T}\varepsilon_{2T} + \varepsilon_{1T}\varepsilon_{3T} + \varepsilon_{2T}\varepsilon_{3T} + \varepsilon_{1T}\varepsilon_{2T}\varepsilon_{3T} \quad (11)$$

T in equation Eq.(11) refer to thermal strains of the resin.

- Calculation of the instantaneous resin specific volume Eq.(12):

$$V_r^{Instant} = V_r^{Start}(1.0 + V_r^T - V_r^C) \quad (12)$$

where V_r^C is the resin specific volume change due to chemical shrinkage.

- Calculation of the instantaneous fiber volume fraction Eq.(13):

$$V_f^{Instant} = 1.0 - V_{void} - V_r^{Instant} \quad (13)$$

Here the assumption is made that the voids volume V_{void} of the part remains constant during the curing cycle.

2.7. Resin Young's modulus

2.7.1. CHILE material model:

Based on the work of Johnston [43], equation (14) was used to describe the evolution of the resin E modulus during cure [56, 57]. The resin instantaneous E modulus is a function of temperature and degree of cure of the resin.

$$E_r = \begin{cases} E_{rmin} & \alpha < \alpha_{gel} \\ E_1 & T^* < T_1 \\ E_2 + (E_1 - E_2) \frac{(T^* - T_2)}{T_1 - T_2} & T_1 \leq T^* < T_2 \\ E_3 + (E_2 - E_3) \frac{(T^* - T_3)}{T_2 - T_3} & T_2 \leq T^* < T_3 \\ E_4 + (E_3 - E_4) \frac{(T^* - T_4)}{T_3 - T_4} & T_3 \leq T^* < T_4 \\ Ae^{-kT^*} & T_4 \leq T^* < T_5 \\ E_5 & T^* > T_5 \end{cases} \quad (14)$$

The quantities $E_1, E_2, E_3, E_4, E_5, A, k, T_1, T_2, T_3, T_4, T_5$ used in Eq.(14) are material constants and E_{rmin} is the E modulus of the resin in the viscous state. Again T is the resin temperature, T_g is the glass transition temperature and T^* can be calculated according to Eq.(4).

To determine the material constants of Eq.(14) for the case of the EPS600 resin, four UD specimens were manufactured and measured in three-point bending test in the DMA apparatus according to ASTM D5023-07 standard. The degree of cure of the tested specimens were 0.927 and the maximum difference of the E-modulus of the specimens measured at the glassy state was less than 3%.

2.7.2. Linear viscoelastic material model:

In order to derive the viscoelastic material properties of the EPS600 resin studied here, dynamic mechanical analysis (DMA) was performed by the Karlsruher Institut of Technology, Institut für technische Mechanik (ITM) on behalf of Premium AEROTEC GmbH. The DMA test was performed at the temperature range of $-30^{\circ}C$ to $250^{\circ}C$ with a temperature step of $5^{\circ}C$ at five discrete frequencies (0.5, 1.58, 5, 15.8 and 50 Hz) per temperature. The degree of cure of the specimens tested was $a_{ref} = 0.94$.

After obtaining the experimental data from the DMA test, master curves were created which describe the viscoelastic behaviour of the material beyond the range of frequencies covered by experimental measurements. The creation of the master curves is based on the time-cure-temperature superposition principle proposed by Simon et.al [53]. According to this principle the effect of temperature and degree of cure on the relaxation times are accounted for by applying the time-temperature superposition principle [49] and the time-cure superposition principle [58, 59].

The time-temperature superposition principle implies that the viscoelastic behaviour at one temperature can be related to that at another temperature by a change in the time scale only [49]. In the case of thermo-rheological simple materials the curves of the instantaneous modulus as a function of time do not change shape as the temperature is changed but appear only to shift left or right. To construct the master curve from the available DMA data the reference temperature T_{ref} was chosen to be equal to the glass transition temperature at the reference degree of cure $T_{ref} = T_g(a_{ref})$. Then the DMA data of the specimens having different temperatures than T_{ref} are shifted horizontally along the frequency axis so that they superimpose with the DMA data of the T_{ref} specimen in order to form a continuous curve.

The empirical relation, first established by Malcolm L. Williams, Robert F. Landel and John D. Ferry also called the Williams-Landel-Ferry or WLF model Eq.(15) was used to calculate the temperature shift factor a_T [60].

$$\log(a_T) = \frac{-C_{g1}(T - T_{ref})}{C_{g2} + (T - T_{ref})} \quad (15)$$

where :

- a_T : Temperature shift factor
- C_{g1}, C_{g2} : Material constants
- T_{ref} : Reference temperature chosen to be equal to the glass transition temperature at the reference degree of cure $T_{ref} = T_g(a_{ref})$
- T : Temperature

The calculation of the C_{g1}, C_{g2} is achieved by curve fitting to the available DMA data. The WLF equation proved to match very well the experimentally derived master curves indicating that the time-temperature superposition principle holds true with the studied resin system.

Similarly to the temperature shift factor a_T , a degree of cure shift factor a_x , accounts for the degree of cure dependence of the relaxation times. In agreement with the work of Simon et.al [53], Plazek et.al [58], Lee et.al [59] we assume that the degree of cure shift factor has a similar form independent of degree of cure if the reference temperature is taken as T_g . Consequently, the degree of cure shift factor a_x in our case is calculated by Eq.(16)

$$\log(a_x) = \frac{-C_{g1}(T_g(a) - T_g^{ref})}{C_{g2} + (T_g(a) - T_g^{ref})} \quad (16)$$

where :

- a_x : Degree of cure shift factor
- C_{g1}, C_{g2} : Material constants as calculated above
- T_g^{ref} : Reference glass transition temperature chosen to be equal to the glass transition temperature at the reference degree of cure $T_g^{ref} = T_g(a_{ref})$

- T_g : Glass transition temperature of the time increment

The combined cure-temperature shift factor can now be calculated from Eq.(15), Eq.(16) as Eq.(17):

$$\log(a_{Tx}) = \log(a_T) + \log(a_x) \quad (17)$$

The result of shifting the experimental data is the creation of two master curves one for the storage modulus E' and one for the loss modulus E'' of the resin. Then the Generalised Maxwell element model Fig. (B.3) was chosen to be fitted to these master curves to describe the viscoelastic material behaviour of the resin [61].

The Generalised Maxwell element model consists of many spring-dashpot Maxwell elements connected in parallel and a spring. The use of many Maxwell elements is done in order to take into account that the relaxation does not occur at a single time, but in a set of times. On the other hand the purpose of the spring is to ensure that the stresses does not fully relax and the viscoelastic material retains a small storage modulus when strain is applied to the material.

The total number (N) of Maxwell elements which are needed by the Generalised Maxwell element model to accurately fit the experimental data depend on the range of frequencies studied. A common practice is to separate the frequency range to N segments at every logarithmic decade and assign to each segment a Maxwell element (spring-dashpot) to model the viscoelastic behaviour. The storage modulus E' and the loss modulus E'' of the studied material can be calculated using Eq.(18).

$$\begin{aligned} E' &= \sum_{i=1}^N E_i \frac{(\omega\tau_i)^2}{1 + (\omega\tau_i)^2} \\ E'' &= \sum_{i=1}^N E_i \frac{\omega\tau_i}{1 + (\omega\tau_i)^2} \end{aligned} \quad (18)$$

where :

- N : Total number of the Maxwell elements
- E_i : The relative stiffness of the i^{th} Maxwell element
- τ_i : Relaxation time of the i^{th} Maxwell element

- ω : The frequency of oscillation
- E', E'' : The experimental value of the storage and loss modulus respectively

To calculate the relative stiffness of every Maxwell element E_i , fitting algorithms were used, the purpose of which is to identify the value of the relative stiffness of the N Maxwell elements that minimise the deviation of the model with the experimental data of the two equations presented in Eq.(18). After determining the relaxation times τ_i and the relative stiffness of every Maxwell element E_i , the resin relaxation tensile modulus can be calculated at every time step of the curing cycle using the Prony series Eq.(19) [61]:

$$E_r(t) = E_{oo} + (E_u - E_{oo}) \sum_{i=1}^N E_i \exp\left(\frac{-t}{a_{Tx}\tau_i}\right) \quad (19)$$

where :

- N : Total number of the Maxwell elements
- $E_r(t)$: The resin relaxation tensile modulus
- E_{oo} : Long term tensile modulus once the material is totally relaxed (equilibrium or rubbery modulus)
- E_u : The unrelaxed resin modulus (glassy modulus)
- E_i : The relative stiffness of the i^{th} Maxwell element
- τ_i : Relaxation time of the i^{th} Maxwell element
- a_{Tx} : Degree of cure - temperature shift factor of the time step
- t : time

The E_{oo} rubbery modulus was set equal to the value of the loss modulus E'' at the highest temperature ($250^\circ C$) and frequency (50 Hz) tested in the DMA analysis. On the other hand at low temperatures the material shows glassy behaviour. As a result the E_u glassy modulus is equal to the storage modulus E' at the lowest temperature ($-30^\circ C$) and highest frequency (50 Hz) tested in the DMA analysis.

2.8. Resin Poisson's coefficient

For the calculation of the resin's instantaneous Poisson's coefficient Eq. (20) was employed [43] :

$$\nu_r(t) = \frac{1}{2} \left(1 - \frac{E_r(t)(1 - 2\nu^\infty)}{E_r^\infty} \right) \quad (20)$$

where :

- ν^∞ : The resin Poisson's ratio at α^∞ ($\alpha = 1.0$)
- E_r^∞ : Resin elastic modulus at α^∞
- $E_r(t)$: Resin Young's modulus.

2.9. Resin G modulus

For the calculation of the resin instantaneous shear modulus $G_r(t)$, Eq. (21) was used assuming isotropic material behaviour :

$$G_r(t) = \frac{E_r(t)}{2(1 + \nu_r(t))} \quad (21)$$

where:

- $\nu_r(t)$: Instantaneous Poisson's coefficient of the resin.
- $E_r(t)$: Resin Young's modulus.

2.10. Lamina engineering constants and expansional coefficients

Having calculated the resin's properties, the next step in the material modelling process is to employ a micromechanics model to derive the mechanical properties and expansional coefficients of the lamina. This is achieved by combining resin and fiber properties assuming orthotropic behaviour for the lamina. The micromechanics model proposed by Bogetti was used to calculate the E and G modulus and the Poisson's ratio ν of the lamina [42]. The mathematical formulations of the model are presented in Appendix A. The definition of the orthotropic stiffness tensor is presented in Appendix B.

2.11. Lamina strains

With the use of the ply expansional coefficients the calculation of the strains of the lamina can be achieved.

The thermal strain of the lamina is calculated with the use of Eq.(22):

$$\boldsymbol{\varepsilon}_{ply}^T = \boldsymbol{\alpha}_{ply}^{CTE} \Delta T \quad (22)$$

where $\boldsymbol{\alpha}_{ply}^{CTE}$ is the coefficient of thermal expansion of the lamina.

The chemical strain of the lamina is calculated with the use of Eq.(23):

$$\boldsymbol{\varepsilon}_{ply}^C = \boldsymbol{\beta}_{ply}^{CSC} \boldsymbol{\varepsilon}_r^C \quad (23)$$

where $\boldsymbol{\beta}_{ply}^{CSC}$ is the chemical shrinkage coefficient of the lamina.

The non mechanical strain of the lamina is the sum of thermal and chemical strain Eq.(24). These strains have opposite sign.

$$\boldsymbol{\varepsilon}_{ply}^{NonMech} = \boldsymbol{\varepsilon}_{ply}^T - \boldsymbol{\varepsilon}_{ply}^C \quad (24)$$

The mechanical strain of the lamina is defined by subtracting from the total ply strains the non mechanical part Eq.(25)

$$\boldsymbol{\varepsilon}_{ply}^{Mech} = \boldsymbol{\varepsilon}_{ply}^{Total} - \boldsymbol{\varepsilon}_{ply}^{NonMech} \quad (25)$$

where:

- ΔT : Increment of temperature
- $\boldsymbol{\varepsilon}_{ply}^{Total}$: Total strain at the end of the current time increment.
- $\boldsymbol{\varepsilon}_r^C$: Resin chemical strain Eq. (8).

2.12. Constitutive equations

2.12.1. CHILE material model

The CHILE material model [43] make use of the generalised Hooke's law constitutive equation Eq.(26), which is a set of analytical equations that relate the stress tensor of the material point ($\boldsymbol{\sigma}_{ij}$), with the corresponding mechanical strain tensor ($\boldsymbol{\varepsilon}_{kl}^{Mech}$), with the use of the elastic stiffness matrix (\boldsymbol{C}_{ijkl}^0).

$$\boldsymbol{\sigma}_{ij} = \sum_k \sum_l \boldsymbol{C}_{ijkl}^0 \boldsymbol{\varepsilon}_{kl}^{Mech} \quad (26)$$

To calculate the mechanical strain tensor ($\boldsymbol{\varepsilon}_{kl}^{Mech}$) and elastic stiffness matrix (\mathbf{C}_{ijkl}^0) of a material point the calculation process depicted in Fig. B.2 is followed. Starting from the calculation of the degree of cure α of the time increment Eq.(1) the calculation progresses to the calculation of the glass transition temperature of the resin Eq.(2) followed by the calculation of the instantaneous resin properties, needed for the homogenization step, namely the instantaneous E, G resin modulus (Eq.(14) and Eq.(21) respectively) and the instantaneous Poisson Eq.(20). The resin's thermal and chemical strains (Eq.(3) to Eq.(8)) and fiber volume fraction coefficient (Eq.(9) to Eq.(13)) can be calculated in parallel and prior to the calculation of the homogenized material point's expansional coefficients and strains.

With the use of the homogenization model proposed by Bogetti [42] (Appendix A) the expansional coefficients (CTE and CSC) (Eq.(A.9) and Eq.(A.10)) and the mechanical strain tensor ($\boldsymbol{\varepsilon}_{kl}^{Mech}$) (Eq.(22) to Eq.(25)) of the material point can be calculated.

The instantaneous elastic (glassy) stiffness matrix (\mathbf{C}_{ijkl}^0) can be calculated from Eq.(B.1) and Eq.(B.2) given as input the effective material properties calculated by the homogenization model (Eq.(A.1) to Eq.(A.8)).

Finally, Eq.(26) is applied to update the stress tensor of the material point. The Consistent Tangent Operator (CTO) to be used by the iterative solution process as depicted in Fig. B.4 is set in the CHILE material model equal to the material point stiffness matrix (\mathbf{C}_{ijkl}^0).

In case each lamina is modelled with one integration point in the thickness direction the above calculation process produces the stress and strain state of the lamina. If more than one integration point in the thickness direction is used (in our case three are used) an output request can be created in ABAQUS based on these integration points to monitor the stress and strain state of the lamina if needed for post processing purposes.

2.12.2. Poon's linear viscoelastic material model

H. Poon et. al developed a constitutive update scheme for simulating anisotropic, thermo rheologically simple, viscoelastic solids [46]. The constitutive equation (27) is proposed by the researchers to calculate the stress tensor of the next time increment.

$$\boldsymbol{\sigma}_{ij}^{n+1}(t) = \sum_k \sum_l \left(\mathbf{C}_{ijkl}^0 \boldsymbol{\varepsilon}_{kl}^{Mech^{n+1}} - \mathbf{D}_{ijkl}^{n+1} \right) \quad (27)$$

The calculation process depicted in Fig. B.2 is also employed in this case.

The starting point is again the calculation of the degree of cure α of the time increment. However, an additional feature here is the calculation of the shift factor of the time increment (Eq.(15) to Eq.(17)) after the calculation of the T_g of the resin. Instead of the use of Eq.(14) for the calculation of the resin instantaneous modulus, Eq.(19) is employed which is the relaxation tensile modulus of the time increment. With the use of the relaxation modulus the Poisson coefficient of the resin Eq.(20) and shear modulus Eq.(21) can be calculated. Then the mechanical strain tensor ($\boldsymbol{\varepsilon}_{kl}^{Mech}$) of the material point is calculated with the use of the resin relaxation modulus (homogenization step Eq.(A.9), Eq.(A.10) and Eq.(22) to Eq.(25)).

The elastic (glassy) stiffness matrix (\mathbf{C}_{ijkl}^0) of a material point is calculated from Eq.(B.1) and Eq.(B.2) given as input the effective glassy stiffness of the material, derived from the homogenization step. In the homogenization step the glassy moduli of the resin is the sum of the stiffness of the Maxwell elements [46].

The state variable \mathbf{D}_{ijkl}^{n+1} is the fictitious creep stress, being defined as the difference between the purely elastic stress based on instantaneous moduli and the actual stress of the material. It is calculated using Eq.(28).

$$\mathbf{D}_{ijkl}^{n+1} = \left[\frac{1}{\Delta t} + \frac{1}{\tau_i a_{Tx}^{n+1}} \right]^{-1} \left[\frac{\mathbf{D}_{ijkl}^n}{\Delta t} + \frac{\tilde{\mathbf{C}}_{ijkl} \boldsymbol{\varepsilon}_{kl}^{Mech^{n+1}}}{\tau_i a_{Tx}^{n+1}} \right] \quad (28)$$

The relaxation stiffness matrix $\tilde{\mathbf{C}}_{ijkl}$ is calculated from Eq.(B.1) and Eq.(B.2) given as input the magnitudes of transient decay of each Maxwell element ((Eu-Eoo)Ei term of Eq.(19)) [46].

The Consistent Tangent Operator (CTO) is calculated using Eq.(29) .

$$\frac{\partial \boldsymbol{\sigma}_{ij}^{n+1}}{\partial \Delta \boldsymbol{\varepsilon}_{ab}} = \mathbf{C}_{ijab}^0 - \frac{\Delta t}{\Delta t + \tau_i a_{Tx}^{n+1}} \tilde{\mathbf{C}}_{ijab} \quad (29)$$

In equations Eq.(27), (28), (29) :

- \mathbf{C}_{ijkl}^0 : Glassy (elastic) stiffness matrix
- $\boldsymbol{\varepsilon}_{kl}^{Mech^{n+1}}$: Mechanical strain tensor
- τ_i : Relaxation time of the i^{th} Maxwell element
- a_{Tx}^{n+1} : Degree of cure - temperature shift factor

- Δt : Time increment
- \tilde{C}_{ijkl} : Relaxation stiffness matrix calculated using as input the transient decay of the Prony series Eq.(19)

3. Experimental procedure

The composite structure that was studied in this research is shown in Fig. B.5. It is a demonstrator frame from the door surround structure of the Airbus A350 aircraft. It is made from Non Crimp Fabric (NCF) by vacuum assisted process infusion as shown in Fig. B.6. The resin system used to manufacture the part was the EPS600 resin supplied by Hexion [62]. The frame is made from UD as well as biax (45/-45) and triax (45/90/-45) fabric of IMS65 fibers, an indeterminate modulus fiber supplied by Toho Tenax. The properties of this fiber can be found in literature [63] or if not explicitly defined by the supplier, can be approximated from the AS4 fiber data published in the literature [43]. The fiber properties used in this research are presented in Table B.1.

The composite frame was manufactured with the use of an inner and outer tool. The female outer tool was made from INVAR alloy and the inner male tool was made from aluminium as shown in Fig. B.7. Fig. B.8 shows the manufacturing process that was followed. The preform was created as shown in Fig. B.9 and then placed on the female mould. The preform was manufactured larger than the final part to allow the machining operations to produce the final geometry of the structure. The aluminium caul was then placed on top of the preform and the whole assembly was put in a vacuum bag.

The curing cycle that was used is depicted in Fig. B.10. Prior to resin infusion the assembly is preheated with a heating rate of $2^{\circ}C/min$ to $120^{\circ}C$ in the oven. In the mean time the resin is also heated from its storage temperature of $-18^{\circ}C$ to $80^{\circ}C$. During this phase the resin transforms from a solid to a liquid phase and its viscosity reduces. When the assembly in the oven reaches $120^{\circ}C$ the resin infusion starts and the resin's viscosity drops further. After the resin infusion is finished, a heat-up phase follows where the assembly is heated to the curing temperature of $180^{\circ}C$ with a heating rate of $1^{\circ}C/min$. When the curing process is over the temperature in the oven drops with a rate of $-2^{\circ}C/min$ until room temperature is reached.

After the curing process was finished the part was taken out of the mould and was checked for manufacturing defects (voids distribution etc). Following

its inspection the composite frame was machined to its final dimensions. The length of the composite frame is around 1769 mm its maximum width is 190 mm and its minimum width 127 mm. The height of the inner flange varies from 30 mm to 40 mm and the height of the outer flange from 75 mm to 30 mm.

After machining, the part was scanned with the use of a 3D scanner and an stl file was created containing the information of the scanned geometry. This was used as reference for comparing the simulation results of the material models. The manufacturing and the 3D scanning of the composite frame took place at the premises of Premium AEROTEC GmbH.

4. Numerical implementation

4.1. Simulation Methodology and boundary conditions

The two material models were implemented in ABAQUS with the use of customized User Material Subroutines (UMAT). The role of this subroutine is to update the stress tensor and CTO of the material integration point that it is called at every time increment of the curing history. Fig. B.4 depicts how UMAT interacts with the ABAQUS solver.

Fig. B.10 depicts the laminate temperature that was used as input in the calculation. It used to approximate the evolution of temperature in the laminate instead of performing a three dimensional heat transfer analysis. It is a product of manufacturing experience, similar to the temperature profiles presented by Svanberg [12], who placed thermocouples at specific locations on the laminate and recorded the temperatures during the curing cycle.

The simulation starts just before the gelation point of the resin and stresses built up earlier in the curing cycle are assumed to contribute insignificantly to the process induced shape distortions of the structure. The curing history was divided into five steps from the gelation point of the resin. These simulation steps along with their imposed boundary conditions are depicted in Table B.2.

In Table B.2 the temperature refers to the temperature at the end of the step. The fixed mechanical boundary condition implies that all the translational Degrees of Freedom (DOFs) of all nodes of the mesh are set to zero displacement. Svanberg concluded that this type of boundary condition is more accurate than the freestanding boundary condition during the curing process [12]. In the demoulding step and the trimming step all DOFs of all nodes are released except of three nodes located at the centerline of the frame, which were used to suppress rigid body motion. Finally, the trimming step refers to the subtraction of a number of elements from the mesh to simulate the machining operations which occur after demoulding the composite part.

The frame consists of six zones as depicted in Fig. B.11. The ply drops offs from one zone to another is 1:20 and the resulting wall thickness of the composite frame ranges from 3.43 mm to 5.76 mm. The biax and triax NCF fabric was modelled with an equivalent number of UD plies at the respective directions by ignoring the stitching of the fabric. Each resulting ply is modelled with the use of three integration points in its thickness direction.

Consequently, the total number of integration points of a zone in the thickness direction is equal to the number of the resulting plies multiplied by three.

4.2. Mesh

Fig. B.11 depicts the finite element mesh that was used to simulate the process induced distortions of the composite frame. It consists of 26433 C3D8I solid elements, which have incompatible modes to improve their bending behaviour [64]. An element length of approximately 5 mm was chosen in the longitudinal and transverse direction. Six elements were used to model the corner between the flanges and the web of the frame. In the thickness direction the composite frame was modelled with one element consisting of multiple integration points according to the stacking sequence of the zone it belongs in order to reduce the computational time. A mesh sensitivity study was carried out with the use of five elements in the thickness direction and the difference was less than 1% compared to the adopted mesh density.

5. Results and Discussion

Given the curing cycle depicted in Fig. B.10 the degree of cure α and the glass transition temperature T_g of the EPS600 resin studied here, are calculated from the gelation to demoulding the structure with the use of Eq.(1),(2) respectively and are presented in Fig. B.12.

The thermal and chemical strain of the resin (Eq.(7),(8)), from the gelation to demoulding the structure is depicted in Fig. B.13. Since the simulation starts at the gelation point the thermal strain slightly increases to a positive value following the laminate temperature profile and then thermal shrinkage occurs as the structure cool down to room temperature. As depicted in Fig. B.13 the chemical strain is negative indicating that chemical shrinkage occurs. The sum of the thermal and chemical strain at any point is the non-mechanical strain experienced by the laminate in through-thickness direction (ε_{33}).

The resulting temperature, cure and the combined cure-temperature shift factor of the resin calculated with the use of Eq.(15),(16),(17) respectively are presented in Fig. B.14.

Fig. B.15 depicts the Young's modulus of the resin, according to the CHILE and the viscoelastic material characterisation. Consequently, the Poisson's coefficient of the resin can be calculated according to Eq.(20) and is presented in Fig. B.16.

Fig. B.17 depicts the distortions induced in the frame after demoulding, with the use of the CHILE and linear viscoelastic material model respectively. The undeformed shape of the frame is shown with the black feature edges surrounding it. The distortion field is multiplied by a factor of 10 in order for the distortions to be visible.

As expected the distortion field increases in magnitude from the web to the flanges. The distance between the flanges is reduced an effect caused by the reduction of the angles between the web and the inner and outer flanges. The viscoelastic material model predicts lower distortions compared to the CHILE material model. The maximum displacement value for the CHILE material model is 1.212 mm whereas for the viscoelastic material model it is 0.975 mm. The simulations also predict that the frame is subjected to warpage. The frame is twisted clockwise while simultaneously it suffers from a downward bending. The greater amount of distortions predicted by the CHILE material model can be attributed to its inability to account for stress relaxation from the gelation point of the structure to cool down.

Fig. B.18 depicts the distortion field of the frame after the trimming process. The trimming process releases residual stresses and the frame springs back to its nominal shape to some extent. The maximum displacement value for the CHILE material model is now 1.117 mm whereas for the viscoelastic material model it is 0.923 mm. Thus, the maximum displacement predicted by the viscoelastic model is around 17% reduced from the value predicted by the CHILE material model. The trimming operation also slightly alters the distribution of distortions in the frame. Therefore a mould geometry compensation approach based on the shape of the part after demoulding but before trimming, will produce inaccurate results. However, because the mould compensation is a non linear process, in other words different geometries produce different amounts of spring-in [2] and the discontinuous distortion field between the trimmed and the untrimmed part, a second verification PID analysis is proposed to verify that the compensated geometry will produce the desired structure.

The difference between the predictions of the two material models is depicted in Fig. B.19. The CHILE material model predicts greater distortions compared to the viscoelastic material model. Red colour indicates outward displacement for the CHILE model to reach the predictions of the viscoelastic material model, whereas blue colour indicates inward displacement.

Here it is important to note that the viscoelastic material model requires around twice the computational time compared to the CHILE material model

mainly because of the increased number of state variables that have to be read from the memory, updated by the material constitutive equation (27) and stored back in memory at every time increment.

Fig. B.20 depicts the distribution of σ_{11} residual stresses predicted by the CHILE and the viscoelastic material model respectively, in the first layer after trimming the frame. As it can be seen residual stresses on the magnitude of 11 MPa are predicted by the CHILE model. In comparison the residual stresses predicted by the viscoelastic material model are 5.6 MPa in magnitude for the first layer of the frame. This can be attributed to some extent to the stress relaxation that the model is able to predict. However, while the residual stresses predicted by the CHILE material model are tensile for the first layer the viscoelastic material model predicts compressive stresses for a significant area of the ply. This fact indicates that the distortion field predicted by the viscoelastic model also results in the redistribution of the internal residuals stresses in the laminate. In any case the residual stresses predicted should be taken into account in the calculation of the reserve factors of the structure.

Before comparing the PID predictions of the two material models with the shape of the manufactured frame, a direct comparison between nominal and manufactured geometry is made as depicted in Fig. B.21.

To enable the comparison between 3D measurements and the CAD geometry or simulation results which is made afterwards, the GOM Inspect suite was used [65]. Since the two databases use different coordinate system an alignment step is necessary in order to perform any comparison. For that purpose the best fit algorithm was used. Since the outer flange of the frame is the one to be fitted to the skin of the aircraft a best fit alignment based on the outer flange and web of the frame was used. For this comparison red colour indicates outward displacement for the nominal geometry to meet the manufactured shape, whereas blue colour indicates inward displacement.

By comparing the nominal shape of the frame with the manufactured one (Fig. B.21) it can be concluded that the flanges of the frame are subjected mainly to spring-in. The magnitude of spring in of the flanges depends on the position of the cross section along the frame. Nine points were placed on the surface of the frame and their deviation to the manufactured frame is depicted in Fig. B.21. The frame also experiences warpage since the web deviates from its nominal position up to 0.93 mm at the back of the frame.

Moreover, as is depicted in Fig. B.18 and Fig. B.21 the measured and calculated distortions of the composite frame in some areas is more than 0.5 mm, which is a typical threshold value used in the industry [2, 6]. Therefore,

manufacturing the composite frame without any compensation will produce a product not meeting its manufacturing specifications.

Fig. B.22 depicts the deviations of the two material models tested from the manufactured part. Red colour indicates outward displacement for the simulation results to reach measurements, whereas blue colour indicates inward displacement.

The viscoelastic simulation framework that was developed predicts more accurately the manufactured shape compared to the CHILE material model, which overestimates the process induced distortions of the frame. This is in agreement with the work presented in the literature [66, 67, 68]. However, in some areas of the frame both the CHILE and the viscoelastic model predict greater distortions compared to those experimentally observed.

The deviation of the simulation results of the viscoelastic material model from the manufactured shape can be attributed to a number of factors and assumptions made in the development of the current simulation framework. A homogeneous temperature field was considered throughout the part, taken as input from manufacturing experience. While this assumption is considered reasonable, due to the small wall thickness of the part and the low heating and cool down rates, small temperature gradients exist in the structure due to the positioning of the mould in the oven, the exothermic heat reaction of the resin, the part shape, the relative motion of the tool part interfaces during cure, and any part warpage that might develop during the cure. These temperature gradients result in property gradients and affect the distortions of the structure.

A sequentially or fully coupled thermal-chemical-mechanical analysis will enable the calculation of the inhomogeneous temperature field distribution and the resulting inhomogeneous curing profile in the part. This approach requires the calculation of the effective thermal properties (conductivity, density and specific heat capacity) of the laminate as a function of temperature and degree of cure. However, further material characterization is required for that purpose.

In addition our viscoelastic model was based on the assumption of thermorheological simplicity, which implies that the retardation spectrum is assumed to not vary with temperature or degree of cure but is simply shifted along the time axis. While this is valid for the time-temperature superposition it not strictly valid for the time-cure superposition [58]. The consideration of thermorheological complex material behaviour would require further material characterisation and the assumption of thermorheological simplicity

is considered a good approximation for modelling the evolution of viscoelastic properties during cure after gelation [53].

Moreover, fabric compaction, permeability and resin flow were not considered in the current modelling approach in order not to increase the modelling complexity and material characterization effort. This leads to the assumption of homogeneous fiber volume fraction and void content in the part during the cure. However, the distribution of the resin in the part at the end of the infusion process is inhomogeneous to some extent depending on many factors such as part shape, local part radius, stacking sequence, the use of single side or two side tooling, positioning of the resin flow medium across the part, fiber bridging, wrinkling and reorientation etc. [52]. These factors cause resin rich and resin poor areas resulting in property gradients in the consolidated laminate affecting process induced distortions and residual stresses. In order to calculate the inhomogeneous resin distribution in the part at the end of the infusion process a resin flow simulation needs to be employed. For that purpose, the resin viscosity as a function of temperature and degree of cure needs to be experimentally measured and modelled.

Furthermore, tool-part interaction was not taken into account in this study and could play a role since the caul plate was made from aluminium to reduce the cost of the experiment. However, as discussed earlier the effect of tool-part interaction cannot be eliminated even with the use of an INVAR tool. Moreover, the biax and triax NCF fabric was modelled as a number of UD plies, neglecting the effect of stitching of the fabric. Also the light projection method used to measure the distortion field of the frame and the creation of the stereolithography file used to make the comparisons is a potential source of error. More importantly the mould and the caul plate that produced the frame were not 3D scanned and their deviation from the nominal CAD geometry is not known.

Finally, another source of error could be the mesh of the frame which is based on de-featured geometry with many geometric details deliberately removed from the CAD geometry to facilitate the meshing operation. This is assumed to be the reason for the characteristic red step observed in the contour plot at the back of the frame and in other areas where there is a ply drop off.

6. Conclusions

The following conclusion can be made from this study:

- The developed viscoelastic simulation framework which employs the linear viscoelastic constitutive update scheme proposed by Harrison Poon and M. Fouad Ahmad [46] and the time-cure-temperature superposition principle proposed by Simon et.al [53] more accurately predicts the manufactured shape compared to the CHILE material model, which overestimates the distortion field of the structure.
- The linear viscoelastic material model needs approximately twice the computational time compared to the CHILE material model to run. Moreover, an increased material characterisation effort is required to derive the viscoelastic material properties needed as input for the material model.
- Since the calculated and measured distortions of the composite frame is more than 0.5 mm, which is a typical threshold value used in the industry [2, 6], manufacturing the product without any compensation will produce a part not meeting its manufacturing specifications.
- A mould geometry compensation approach based on the shape of the part after demoulding will produce inaccurate results as the trimming operations which usually take place in the industry, release stresses that affect the distortion field of the structure, depending on the extent of these operations.
- Residual stresses exist in the final product and should be taken into account in the calculation of the reserve factors of the structure.
- The use of viscoelastic material models is proposed if the objective is to increase the accuracy of the employed simulation framework in the prediction of process induced distortions of aerospace thermoset composite structures.

Future work will focus on performing a heat transfer analysis to more accurately determine the temperature field in the part. This could serve as input in the developed simulation framework to further improve its accuracy.

Finally, with the aim to substitute the expensive INVAR tools conventionally used in the aerospace industry and replace them with low cost steel or aluminium alloys, tool part interaction will be investigated and the effect and applicability of various friction models on the developed simulation framework of process induced distortions of aerospace thermoset composite structures will be assessed.

7. Acknowledgements

This work has received funding from the European Union’s Horizon 2020 research and innovation programme under the Marie Skłodowska-Curie grant agreement No 764650. It is part of the OptiMACS project performing research in the field of optimization of multifunctional aerospace composite structures.

8. Nomenclature

- $\dot{\alpha}$: Degree of cure rate
- α : Degree of cure
- α^{gel} : The degree of cure at the gelation point of the resin
- α^0 : The degree of cure at $\alpha = 0$
- α^∞ : The degree of cure at $\alpha = 1$
- R : Universal gas constant
- T : Temperature
- A_1, A_2 : Arrhenius constants
- E_{a1}, E_{a2} : Activation energies of the autocatalytic models
- $m_1, n_1, C, \alpha_{c0}, \alpha_{cT}, m_2, n_2$: Material constants used by the cure kinetics equation
- T_g : Glass transition temperature
- λ : DiBenedetto material parameter

- T_g^0 : Glass transition temperature at α^0
- T_g^∞ : Glass transition temperature at α^∞
- α_r^{CTE} : Coefficient of thermal expansion of the resin second order tensor.
- T^* : Temperature difference to the glass transition temperature.
- $\alpha_{rub}^{CTE}, \alpha_{glass}^{CTE}$: Coefficient of thermal expansion of the resin second order tensor at the rubbery and glassy state respectively.
- $T_{C1}, T_{C2}, C_2, C_3, C_4, \alpha_\alpha$: Material constants used for the calculation of the CTE of the resin.
- V_r^C : Volumetric chemical shrinkage of the resin second order tensor.
- $V_r^{C\infty}$: Maximum volumetric chemical shrinkage of the resin second order tensor at α^∞ .
- $B, \alpha_{c1}, \alpha_{c2}$: Material constants used for the calculation of the volumetric chemical shrinkage of the resin.
- α_c : Degree of cure fraction
- ϵ_r^T : Resin thermal strain second order tensor.
- ϵ_r^C : Resin chemical strain second order tensor.
- V_r^{Final} : Specific volume of the resin in the final product
- V_r^{Start} : Specific volume of the resin at the start of the manufacturing process
- V_{void} : Specific volume of the voids in the final product.
- V_f^{Final} : Fiber volume fraction of the final product.
- V_r^T : Specific volume change of the resin due to thermal strains
- $V_r^{Instant}$: Instantaneous specific volume of the resin
- $V_f^{Instant}$: instantaneous fiber volume fraction

- E_r : Resin Young's modulus according to the CHILE material model
- E_{rmin} : The E modulus of the resin in the viscous state
- $E_1, E_2, E_3, E_4, E_5, A, k, T_1, T_2, T_3, T_4, T_5$: Material constants used by the CHILE material model
- a_T : Temperature shift factor
- a_x : Degree of cure shift factor
- a_{Tx} : Degree of cure-temperature shift factor
- C_{g1}, C_{g2} : Fitting parameters of the WLF equation
- T_{ref} : Reference temperature used for the temperature shift factor
- T_g^{ref} : Reference glass transition temperature used for the degree of cure shift factor
- E', E'' : DMA values of the storage and loss modulus respectively
- N : Total number of the Maxwell elements
- E_i : The relative stiffness of the i^{th} Maxwell element
- τ_i : Relaxation time of the i^{th} Maxwell element
- ω : The frequency of oscillation
- $E_r(t)$: Relaxation tensile modulus of the resin
- E_{oo} : Long term tensile modulus once the material is totally relaxed (equilibrium or rubbery modulus)
- E_u : The unrelaxed resin modulus (glassy modulus)
- t : time
- $\nu_r(t)$: Instantaneous Poisson's coefficient of the resin
- ν^∞ : The resin Poisson's ratio at α^∞
- E_r^∞ : Resin Young's modulus at α^∞

- $G_r(t)$: Resin instantaneous shear modulus
- α_{ply}^{CTE} : Coefficient of thermal expansion of the lamina second order tensor.
- β_{ply}^{CSC} : Chemical shrinkage coefficient of the lamina second order tensor.
- ϵ_{ply}^T : Second order thermal strain tensor of the lamina
- ϵ_{ply}^C : Second order chemical strain tensor of the lamina
- $\epsilon_{ply}^{NonMech}$: Second order non-mechanical strain tensor of the lamina
- ϵ_{ply}^{Mech} : Second order mechanical strain tensor of the lamina
- ϵ_{ply}^{Total} : Second order total strain tensor of the lamina.
- σ_{ij} : Second order stress tensor
- D_{ijkl} : Fictitious creep stress second order tensor
- C_{ijkl}^0 : Glassy fourth order stiffness tensor
- \tilde{C}_{ijkl} : Relaxation fourth order stiffness tensor calculated using as input the transient decay of the Prony series Eq.(19)

Appendix A. Micromechanics model

The lamina's mechanical properties namely the E and G modulus and the lamina's Poisson ratio ν were calculated according to the formulations proposed by Bogetti [42].

In the following equations :

- The variables having the subscript f refer to fiber properties
- The variables having the subscript m refer to matrix properties
- The subscript 1 refer to the longitudinal direction of the lamina
- The subscripts 2 3 refer to the transverse directions 2, 3 of the lamina respectively

- ν is the Poisson's coefficient in the respective directions
- ν_f is the fiber volume fraction of the lamina
- E is the Young's modulus
- G is the shear modulus

The variable k Eq.(A.1) is referred as isotropic plane strain bulk modulus :

$$k = \frac{E}{2(1 - \nu - 2\nu^2)} \quad (\text{A.1})$$

The longitudinal Young's modulus of the lamina is defined as Eq.(A.2) :

$$E_1 = E_{1f}\nu_f + E_{1m}(1 - \nu_f) + \frac{4(\nu_{12m} - \nu_{12f}^2)k_f k_m G_{23m}(1 - \nu_f)\nu_f}{(k_f + G_{23m})k_m + (k_f - k_m)G_{23m}\nu_f} \quad (\text{A.2})$$

The major Poisson's ratio Eq.(A.3):

$$\nu_{12} = \nu_{13} = \nu_{12f}\nu_f + \nu_{12m}(1 - \nu_f) + \frac{(\nu_{12m} - \nu_{12f})(k_m - k_f)G_{23m}(1 - \nu_f)\nu_f}{(k_f + G_{23m})k_m + (k_f - k_m)G_{23m}\nu_f} \quad (\text{A.3})$$

The inplane shear modulus Eq.(A.4):

$$G_{12} = G_{13} = G_{12m} \frac{(G_{12f} + G_{12m}) + (G_{12f} - G_{12m})\nu_f}{(G_{12f} + G_{12m}) - (G_{12f} - G_{12m})\nu_f} \quad (\text{A.4})$$

The transverse shear modulus Eq.(A.5):

$$G_{23} = \frac{G_{23m}[k_m(G_{23m} + G_{23f}) + 2G_{23f}G_{23m} + k_m(G_{23f} - G_{23m})\nu_f]}{k_m(G_{23m} + G_{23f}) + 2G_{23f}G_{23m} - (k_m + 2G_{23m})(G_{23f} - G_{23m})\nu_f} \quad (\text{A.5})$$

The effective plane strain bulk modulus of the composite ply Eq.(A.6):

$$k_T = \frac{(k_f + G_{23m})k_m + (k_f - k_m)G_{23m}\nu_f}{(k_f + G_{23m}) - (k_f - k_m)\nu_f} \quad (\text{A.6})$$

The transverse Young's modulus Eq.(A.7):

$$E_2 = E_3 = \frac{1}{\frac{1}{4k_T} + \frac{1}{4G_{23}} + \frac{\nu_{12}^2}{E_1}} \quad (\text{A.7})$$

The transverse Poisson's ratio Eq.(A.8):

$$\nu_{23} = \frac{2_1k_T - E_1E_2 - 4\nu_{12}^2k_{T2}}{2_1k_T} \quad (\text{A.8})$$

Appendix A.1. Lamina expansional coefficients:

The lamina expansional coefficients were also calculated according to the formulations proposed by Bogetti [42].

The longitudinal expansional strain of the ply Eq.(A.9):

$$\varepsilon_1 = \frac{\varepsilon_{1f}E_{1f}\nu_f + \varepsilon_{1m}E_{1m}(1 - \nu_f)}{E_{1f}\nu_f + E_{1m}(1 - \nu_f)} \quad (\text{A.9})$$

The transverse expansional strain of the ply Eq.(A.10):

$$\varepsilon_2 = \varepsilon_3 = (\varepsilon_{2f} + \nu_{12f}\varepsilon_{1f})\nu_f + (\varepsilon_{2m} + \nu_{12m}\varepsilon_{1m})(1 - \nu_f) - (\nu_{12f}\nu_f + \nu_{12m}(1 - \nu_f))\varepsilon_1 \quad (\text{A.10})$$

In order to calculate from Eq.(A.9) and Eq.(A.10) the CTE of the ply (α_{ply}^{CTE}) the expansional strains of the fiber and matrix ($\varepsilon_{1f}, \varepsilon_{1m}, \varepsilon_{2f}$ etc.) are substituted by the CTE coefficients of the materials in the relevant directions.

Regarding the calculation of the CSC of the ply (β_{ply}^{CSC}), the expansional strains of the fiber ($\varepsilon_{1f}, \varepsilon_{2f}$) are set equal to zero as the fiber naturally does not chemically react. The expansional strains of the matrix ($\varepsilon_{1m}, \varepsilon_{2m}$) are set equal to one.

Appendix B. Stiffness matrix

Orthotropic material behaviour is assumed for the lamina. The orthotropic stiffness matrix \mathbf{C} has the following definition Eq.(B.1) [64]:

$$\mathbf{C} = \begin{bmatrix} C_{11} & C_{12} & C_{13} & 0 & 0 & 0 \\ C_{12} & C_{22} & C_{23} & 0 & 0 & 0 \\ C_{13} & C_{23} & C_{33} & 0 & 0 & 0 \\ 0 & 0 & 0 & C_{44} & 0 & 0 \\ 0 & 0 & 0 & 0 & C_{55} & 0 \\ 0 & 0 & 0 & 0 & 0 & C_{66} \end{bmatrix} \quad (\text{B.1})$$

where :

$$\begin{aligned} C_{11} &= E_1(1 - \nu_{23}\nu_{32})\Upsilon \\ C_{22} &= E_2(1 - \nu_{13}\nu_{31})\Upsilon \\ C_{33} &= E_3(1 - \nu_{12}\nu_{21})\Upsilon \\ C_{12} &= E_1(\nu_{21} + \nu_{31}\nu_{23})\Upsilon \\ C_{13} &= E_1(\nu_{31} + \nu_{21}\nu_{32})\Upsilon \\ C_{23} &= E_2(\nu_{32} + \nu_{12}\nu_{31})\Upsilon \\ C_{44} &= G_{12} \\ C_{55} &= G_{13} \\ C_{66} &= G_{23} \\ \Upsilon &= \frac{1}{1 - \nu_{12}\nu_{21} - \nu_{23}\nu_{32} - \nu_{31}\nu_{13} - 2\nu_{21}\nu_{32}\nu_{13}} \end{aligned} \quad (\text{B.2})$$

To derive the isotropic stiffness matrix for the calculation of the resin's fictitious creep stresses according to Eq.(28) of the linear viscoelastic material model proposed by H. Poon, the stiffness constituents have the following definition Eq.(B.3).

$$\begin{aligned} C_{11} &= \Upsilon(1 - \nu) \\ C_{11} &= C_{22} = C_{33} \\ C_{12} &= \Upsilon\nu \\ C_{12} &= C_{13} = C_{23} \\ C_{44} &= \frac{1 - 2\nu}{2} \\ C_{44} &= C_{55} = C_{66} \\ \Upsilon &= \frac{E}{(1 + \nu)(1 - 2\nu)} \end{aligned} \quad (\text{B.3})$$

References

- [1] C. Albert, G. Fernlund, Spring-in and warpage of angled composite laminates, *Composites Science and Technology* 62 (14) (2002) 1895-1912. doi:[https://doi.org/10.1016/S0266-3538\(02\)00105-7](https://doi.org/10.1016/S0266-3538(02)00105-7).
- [2] E. Kappel, Compensating process-induced distortions of composite structures: A short communication, *Composite Structures* 192 (2018) 67–71. doi:<https://doi.org/10.1016/j.compstruct.2018.02.059>.
- [3] G. Fernlund, A. Osooly, A. Poursartip, R. Vaziri, R. Courdji, K. Nelson, P. George, L. Hendrickson, J. Griffith, Finite element based prediction of process-induced deformation of autoclaved composite structures using 2d process analysis and 3d structural analysis, *Composite Structures* 62 (2) (2003) 223–234. doi:[https://doi.org/10.1016/S0263-8223\(03\)00117-X](https://doi.org/10.1016/S0263-8223(03)00117-X).
- [4] M. Fiorina, A. Seman, B. Castanie, K. Ali, C. Schwob, L. Mezeix, Spring-in prediction for carbon/epoxy aerospace composite structure, *Composite Structures* 168 (2017) 739–745. doi:<http://dx.doi.org/10.1016/j.compstruct.2017.02.074>.
- [5] E. Kappel, D. Stefaniak, D. Holzhter, C. Hhne, M. Sinapius, Manufacturing distortions of a cfrp box-structure a semi-numerical prediction approach, *Composites Part A: Applied Science and Manufacturing* 51 (2013) 89–98. doi:<http://dx.doi.org/10.1016/j.compositesa.2013.04.003>.
- [6] E. Kappel, A zone-based approach to predict process-induced distortions of composite structures based on a 'spring-in reference curve', *Composite Structures* 209 (2019) 143–149. doi:<https://doi.org/10.1016/j.compstruct.2018.10.045>.
- [7] B. Wucher, F. Lani, T. Pardoën, C. Bailly, P. Martiny, Tooling geometry optimization for compensation of cure-induced distortions of a curved carbon/epoxy c-spar, *Composites Part A: Applied Science and Manufacturing* 56 (2014) 27–35. doi:<http://dx.doi.org/10.1016/j.compositesa.2013.09.010>.
- [8] E. Kappel, D. Stefaniak, C. Hhne, Process distortions in prepreg manufacturing an experimental study on

- cfRP l-profiles, *Composite Structures* 106 (2013) 615–625. doi:<http://dx.doi.org/10.1016/j.compstruct.2013.07.020>.
- [9] N. Ersoy, T. Garstka, K. Potter, M. R. Wisnom, D. Porter, G. Stringer, Modelling of the spring-in phenomenon in curved parts made of a thermosetting composite, *Composites Part A: Applied Science and Manufacturing* 41 (2010) 410–418. doi:[doi:10.1016/j.compositesa.2009.11.008](https://doi.org/10.1016/j.compositesa.2009.11.008).
- [10] C. Bellini, L. Sorrentino, W. Polini, A. Corrado, Spring-in analysis of cfRP thin laminates: numerical and experimental results, *Composite Structures* 173 (2017) 17–24. doi:<http://dx.doi.org/10.1016/j.compstruct.2017.03.105>.
- [11] L. Mezeix, A. Seman, M. Nasir, Y. Aminanda, A. Rivai, B. Castani, P. Olivier, K. Ali, Spring-back simulation of unidirectional carbon/epoxy flat laminate composite manufactured through autoclave process, *Composite Structures* 124 (2015) 196–205. doi:<http://dx.doi.org/10.1016/j.compstruct.2015.01.005>.
- [12] J. M. Svanberg, Predictions of manufacturing induced shape distortions, Lulea University of Technology, 2002.
- [13] E. Kappel, Forced-interaction and spring-in relevant initiators of process-induced distortions in composite manufacturing, *Composite Structures* 140 (2016) 217–229. doi:<http://dx.doi.org/10.1016/j.compstruct.2016.01.016>.
- [14] X. Zeng, J. Raghavan, Role of tool-part interaction in process-induced warpage of autoclave-manufactured composite structures, *Composites Part A: Applied Science and Manufacturing* 41 (2010) 1174–1183. doi:<https://doi.org/10.1016/j.compositesa.2010.04.017>.
- [15] D. Stefaniak, E. Kappel, T. Sprwitz, C. Hhne, Experimental identification of process parameters inducing warpage of autoclave-processed cfRP parts, *Composites Part A: Applied Science and Manufacturing* 43 (7) (2012) 1081–1091. doi:<http://dx.doi.org/10.1016/j.compositesa.2012.02.013>.
- [16] L. Sun, J. Wang, A. Ni, S. Li, A. Ding, Modelling and experiment of process-induced distortions in unsymmetrical

- laminate plates, *Composite Structures* 182 (2017) 524–532.
doi:<http://dx.doi.org/10.1016/j.compstruct.2017.09.018>.
- [17] N. Ersoy, K. Potter, M. R. Wisnom, M. J. Clegg, Development of spring-in angle during cure of a thermosetting composite, *Composites Part A: Applied Science and Manufacturing* 36 (12) (2005) 1700–1706.
doi:<http://dx.doi.org/10.1016/j.compositesa.2005.02.013>.
- [18] E. Kappel, R. Prussak, On abnormal thermal-expansion properties of more orthotropic m21e/ima carbon-fiber-epoxy laminates, *Composites Communications* 17 (2020) 129–133.
doi:<https://doi.org/10.1016/j.coco.2019.11.014>.
- [19] K.-T. Hsiao, S. Gangireddy, Investigation on the spring-in phenomenon of carbon nanofiber-glass fiber/polyester composites manufactured with vacuum assisted resin transfer molding, *Composites Part A: Applied Science and Manufacturing* 39 (2008) 834–842.
doi:<https://doi.org/10.1016/j.compositesa.2008.01.015>.
- [20] C. Dong, Process-induced deformation of composite t-stiffener structures, *Composite Structures* 92 (2010) 1614–1619.
doi:<https://doi.org/10.1016/j.compstruct.2009.11.026>.
- [21] E. Kappel, Spring-in of curved cfrp/foam-core sandwich structures, *Composite Structures* 128 (2015) 155–164.
doi:<http://dx.doi.org/10.1016/j.compstruct.2015.03.058>.
- [22] Y. Mahadik, K. Potter, Experimental investigation into the thermoelastic spring-in of curved sandwich panels, *Composites Part A: Applied Science and Manufacturing* 49 (2013) 68–80.
doi:<http://dx.doi.org/10.1016/j.compositesa.2013.02.006>.
- [23] D. Radford, T. Rennick, Separating sources of manufacturing distortion in laminated composites, *Journal of Reinforced Plastics and Composites* 19 (8) (2000) 621–641.
- [24] M. Wisnom, K. Potter, N. Ersoy, Shear-lag analysis of the effect of thickness on spring-in of curved composites, *Journal of Composite Materials* 41 (11) (2007) 1311–1324.

- [25] A. Ding, S. Li, J. Wang, A. Ni, A new analytical solution for spring-in of curved composite parts, *Composites Science and Technology* 142 (2017) 30–40. doi:<http://dx.doi.org/10.1016/j.compscitech.2017.01.024>.
- [26] A. R. A. Arafath, R. Vaziri, A. Poursartip, Closed-form solution for process-induced stresses and deformation of a composite part cured on a solid tool: Part i flat geometries, *Composites Part A: Applied Science and Manufacturing* 39 (2008) 1106–1117. doi:<https://doi.org/10.1016/j.compositesa.2008.04.009>.
- [27] A. R. A. Arafath, R. Vaziri, A. Poursartip, Closed-form solution for process-induced stresses and deformation of a composite part cured on a solid tool: Part ii curved geometries, *Composites Part A: Applied Science and Manufacturing* 40 (2009) 1545–1557. doi:<https://doi.org/10.1016/j.compositesa.2009.01.009>.
- [28] E. Kappel, D. Stefaniak, T. Sprwitz, C. Hhne, A semi-analytical simulation strategy and its application to warpage of autoclave-processed cfrp parts, *Composites Part A: Applied Science and Manufacturing* 42 (2011) 1985–1994. doi:<https://doi.org/10.1016/j.compositesa.2011.09.001>.
- [29] E. Kappel, D. Stefaniak, G. Fernlund, Predicting process-induced distortions in composite manufacturing a pheno-numerical simulation strategy, *Composite Structures* 120 (2015) 98–106. doi:<http://dx.doi.org/10.1016/j.compstruct.2014.09.069>.
- [30] A. Ding, S. Li, J. Wang, A. Ni, L. Zu, A new path-dependent constitutive model predicting cure-induced distortions in composite structures, *Composites Part A: Applied Science and Manufacturing* 95 (2017) 183–196. doi:<http://dx.doi.org/10.1016/j.compositesa.2016.11.032>.
- [31] M. Abouhamzeh, J. Sinke, K. Jansen, R. Benedictus, A new procedure for thermo-viscoelastic modelling of composites with general orthotropy and geometry, *Composite Structures* 133 (2015) 871–877. doi:<http://dx.doi.org/10.1016/j.compstruct.2015.08.050>.
- [32] P. Hubert, A. Poursartip, A review of flow and compaction modelling relevant to thermoset matrix laminate processing, *Journal of Reinforced Plastics and Composites* 17 (4) (1998) 286–318. doi:<https://doi.org/10.1177/073168449801700402>.

- [33] J. Lightfoot, M. Wisnom, K. Potter, A new mechanism for the formation of ply wrinkles due to shear between plies, *Composites Part A-applied Science and Manufacturing* 49 (2013) 139–147.
- [34] K. Potter, C. Langer, B. Hodgkiss, S. Lamb, Sources of variability in uncured aerospace grade unidirectional carbon fibre epoxy prepreg, *Composites Part A: Applied Science and Manufacturing* 38 (3) (2007) 905 – 916. doi:<https://doi.org/10.1016/j.compositesa.2006.07.010>.
- [35] E. Lamers, Shape distortions in fabric reinforced composite products due to processing induced fibre reorientation, Ph.D. thesis, Netherlands (apr 2004).
- [36] M. Benavente, L. Marcin, A. Courtois, M. Lvesque, E. Ruiz, Numerical analysis of viscoelastic process-induced residual distortions during manufacturing and post-curing, *Composites Part A: Applied Science and Manufacturing* 107 (2018) 205–216. doi:<https://doi.org/10.1016/j.compositesa.2018.01.005>.
- [37] W. Chen, D. Zhang, A micromechanics-based processing model for predicting residual stress in fiber-reinforced polymer matrix composites, *Composite Structures* 204 (2018) 153–166. doi:<https://doi.org/10.1016/j.compstruct.2018.07.016>.
- [38] B. Tavakol, P. Roozbehjavan, A. Ahmed, R. Das, R. Joven, H. Koushyar, A. Rodriguez, B. Minaie, Prediction of residual stresses and distortion in carbon fiber-epoxy composite parts due to curing process using finite element analysis, *Journal of Applied Polymer Science* 128 (2) (2013) 941–950. arXiv:<https://onlinelibrary.wiley.com/doi/pdf/10.1002/app.38075>, doi:<https://doi.org/10.1002/app.38075>.
- [39] A. Ding, S. Li, J. Wang, L. Zu, A three-dimensional thermo-viscoelastic analysis of process-induced residual stress in composite laminates, *Composite Structures* 129 (2015) 60–69. doi:<http://dx.doi.org/10.1016/j.compstruct.2015.03.034>.
- [40] A. Ding, S. Li, J. Sun, J. Wang, L. Zu, A thermo-viscoelastic model of process-induced residual stresses in composite structures with considering thermal dependence, *Composite Structures* 136 (2016) 34–43. doi:<http://dx.doi.org/10.1016/j.compstruct.2015.09.014>.

- [41] J. Zhang, M. Zhang, S. Li, M. Pavier, D. Smith, Residual stresses created during curing of a polymer matrix composite using a viscoelastic model, *Composites Science and Technology* 130 (2016) 20–27. doi:<http://dx.doi.org/10.1016/j.compscitech.2016.05.002>.
- [42] T. A. Bogetti, J. W. Gillespie, Process-induced stress and deformation in thick-section thermoset composite laminates, *Journal of Composite Materials* 26 (5) (1992) 626–660. doi:<https://doi.org/10.1177/002199839202600502>.
- [43] A. A. Johnston, An integrated model of the development of process-induced deformation in autoclave processing of composite structures, Ph.D. thesis, University of British Columbia (1997). doi:<http://dx.doi.org/10.14288/1.0088805>.
- [44] G. Zhang, J. Wang, A. Ni, H. Hu, A. Ding, S. Li, Process-induced deformation of l - shaped variable-stiffness composite structures during cure, *Composite Structures* 230 (111461). doi:<https://doi.org/10.1016/j.compstruct.2019.111461>.
- [45] M. A. Zocher, S. E. Groves, A three dimensional finite element formulation for thermoviscoelastic orthotropic media, *International Journal for Numerical Methods in Engineering* 40 (12) (1997) 2267–2288. doi:[https://doi.org/10.1002/\(SICI\)1097-0207\(19970630\)40:12<2267::AID-NME156>3.0.CO;2-P](https://doi.org/10.1002/(SICI)1097-0207(19970630)40:12<2267::AID-NME156>3.0.CO;2-P)—.
- [46] H. Poon, M. F. Ahmad, A material point time integration procedure for anisotropic, thermo rheologically simple, viscoelastic solids, *Computational Mechanics* 21 (3) (1998) 236–242. doi:<https://doi.org/10.1007/s004660050298>.
- [47] H. Poon, M. F. Ahmad, A finite element constitutive update scheme for anisotropic, viscoelastic solids exhibiting non-linearity of the schapery type, *International Journal for Numerical Methods in Engineering* 46 (12) (1999) 2027–2041. doi:[https://doi.org/10.1002/\(SICI\)1097-0207\(19991230\)46:12<2027::AID-NME575>3.0.CO;2-5](https://doi.org/10.1002/(SICI)1097-0207(19991230)46:12<2027::AID-NME575>3.0.CO;2-5).
- [48] R. Schapery, On the characterization of nonlinear viscoelastic materials, *Polymer Engineering and Science* 9 (4) (1969) 295–310. doi:<https://doi.org/10.1002/pen.760090410>—.

- [49] Y. Eom, L. Boogh, V. Michaud, P. Sunderland, J.-A. Manson, Time-cure-temperature superposition for the prediction of instantaneous viscoelastic properties during cure, *Polymer Engineering and Science* 40 (6) (2000) 1281–1292. doi:<https://doi.org/10.1002/pen.11256>.
- [50] D. J. O’Brien, P. T. Mather, S. R. White, Viscoelastic properties of an epoxy resin during cure, *Journal of Composite Materials* 35 (10) (2001) 883–904. doi:<https://doi.org/10.1106/HLYM-5CM7-BP9N-L1Y1>.
- [51] M. Benavente, L. Marcin, A. Courtois, M. Lvesque, E. Ruiz, Viscoelastic distortion in asymmetric plates during post curing, *Composites Part A: Applied Science and Manufacturing* 103 (2017) 122–130. doi:<https://doi.org/10.1016/j.compositesa.2017.09.017>.
- [52] N. E. R. A. J. H. H. Ismet Baran, Kenan Cinar, A review on the mechanical modeling of composite manufacturing processes., *Arch Computat Methods Eng* 24 (2017) 365–395. doi:<https://doi.org/10.1007/s11831-016-9167-2>.
- [53] O. S. Sindee L. Simon, Gregory B. Mckenna, Modeling the evolution of the dynamic mechanical properties of a commercial epoxy during cure after gelation, *Journal of Applied Polymer Science* 76 (2000) 495–508. doi:[https://doi.org/10.1002/\(SICI\)1097-4628\(20000425\)76:4<495::AID-APP7;3.0.CO;2-B](https://doi.org/10.1002/(SICI)1097-4628(20000425)76:4<495::AID-APP7;3.0.CO;2-B).
- [54] S.-N. Lee, M.-T. Chiu, H.-S. Lin, Kinetic model for the curing reaction of a tetraglycidyl diamino diphenyl methane/diamino diphenyl sulfone (tgddm/dds) epoxy resin system, *Polymer Engineering & Science* 32 (15) (1992) 1037–1046. doi:<https://doi.org/10.1002/pen.760321509>.
- [55] K. C. Cole, J. J. Hechler, D. Noel, A new approach to modeling the cure kinetics of epoxy/amine thermosetting resins. 2. application to a typical system based on bis[4-(diglycidylamino)phenyl]methane and bis(4-aminophenyl) sulfone, *Macromolecules* 24 (11) (1991) 3098–3110. doi:<https://doi.org/10.1021/ma00011a012>.
- [56] J. Weiland, Eps600 charakterisierung: Abschlussbericht, TUM Lehrstuhl für Carbon Composites, 2017.
- [57] Compro model documentation v1.3., Convergent Manufacturing Technologies.

- [58] D. J. Plazek, I.-C. Chay, The evolution of the viscoelastic retardation spectrum during the development of an epoxy resin network, *Journal of Polymer Science Part B: Polymer Physics* 29 (1) (1991) 17–29. doi:<https://doi.org/10.1002/polb.1991.090290104>.
- [59] A. Lee, G. B. McKenna, Effect of crosslink density on physical ageing of epoxy networks, *Polymer* 29 (10) (1988) 1812–1817. doi:[https://doi.org/10.1016/0032-3861\(88\)90396-5](https://doi.org/10.1016/0032-3861(88)90396-5).
- [60] M. L. Williams, R. F. Landel, J. D. Ferry, The temperature dependence of relaxation mechanisms in amorphous polymers and other glass-forming liquids, *Journal of the American Chemical Society* 77 (14) (1955) 3701–3707. doi:<https://doi.org/10.1021/ja01619a008>.
- [61] D. Roylance, *Engineering viscoelasticity*, Massachusetts Institute of Technology, 2001.
- [62] Technical data sheet epikote system 600, HEXION.
- [63] Delivery programme and characteristics for tenax ims65 filament yarn, Toho Tenax, 2010.
- [64] Abaqus analysis user’s guide version 6.14, Dassault Systemes Simulia Corp, 2014.
- [65] <https://www.gom.com/en/products/gom-inspect-suite>.
- [66] L. Khoun, R. de Oliveira, V. Michaud, P. Hubert, Investigation of process-induced strains development by fibre bragg grating sensors in resin transfer moulded composites, *Composites Part A: Applied Science and Manufacturing* 42 (2011) 274–282. doi:<https://doi.org/10.1016/j.compositesa.2010.11.013>.
- [67] M. W. Nielsen, J. W. Schmidt, J. H. Hattel, T. L. Andersen, C. M. Markussen, In situ measurement using fbgs of process-induced strains during curing of thick glass/epoxy laminate plate: experimental results and numerical modelling, *Wind Energy* 16 (8) (2013) 1241–1257. doi:<https://doi.org/10.1002/we.1550>.

- [68] W. Chen, D. Zhang, Improved prediction of residual stress induced warpage in thermoset composites using a multi-scale thermo-viscoelastic processing model, *Composites Part A: Applied Science and Manufacturing* 126 (2019) 105575. doi:<https://doi.org/10.1016/j.compositesa.2019.105575>.

Figure Captions

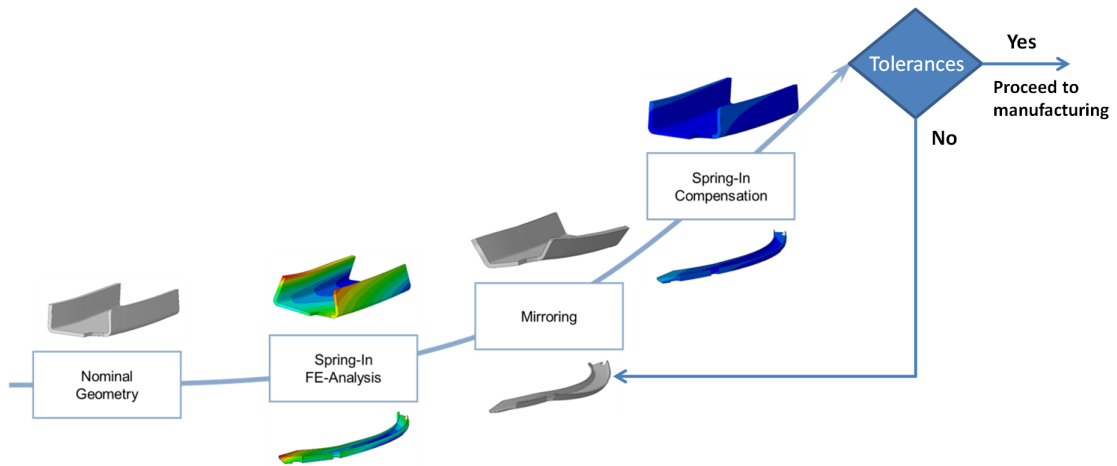


Figure B.1: Typical design process of new moulds with the use of the mould geometry compensation approach. The Process Induced Distortions (PID) of the nominal geometry are simulated by employing a material model. The resulting deformation field is reversed in the mirroring step to serve as a compensated tool geometry. Then an additional PID simulation is executed to verify that the expected distortions lie in the tolerance range of the part.

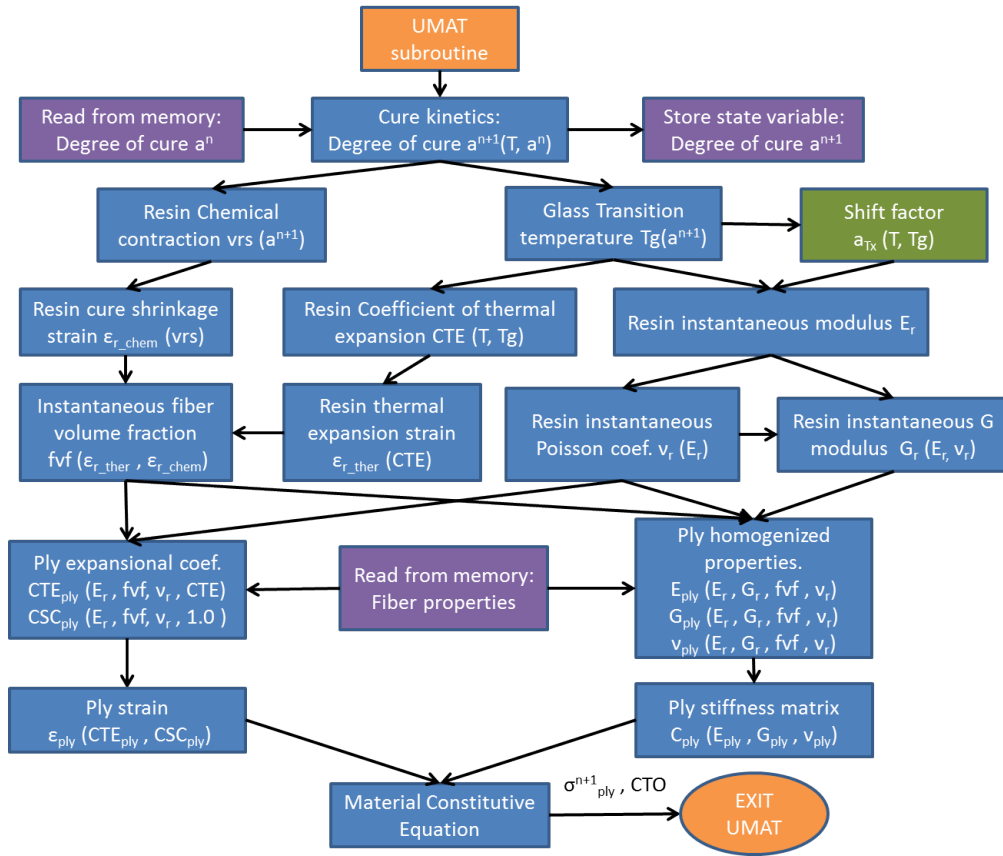


Figure B.2: Flowchart of the material modelling architecture. Blue colour indicates variable calculation, purple access of memory, orange start/finish of the calculation process whereas the green box is employed only by the viscoelastic material model.

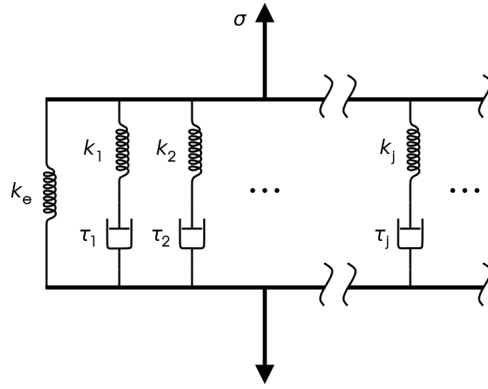


Figure B.3: Generalised Maxwell element consisting of many spring-dashpot Maxwell elements [61].

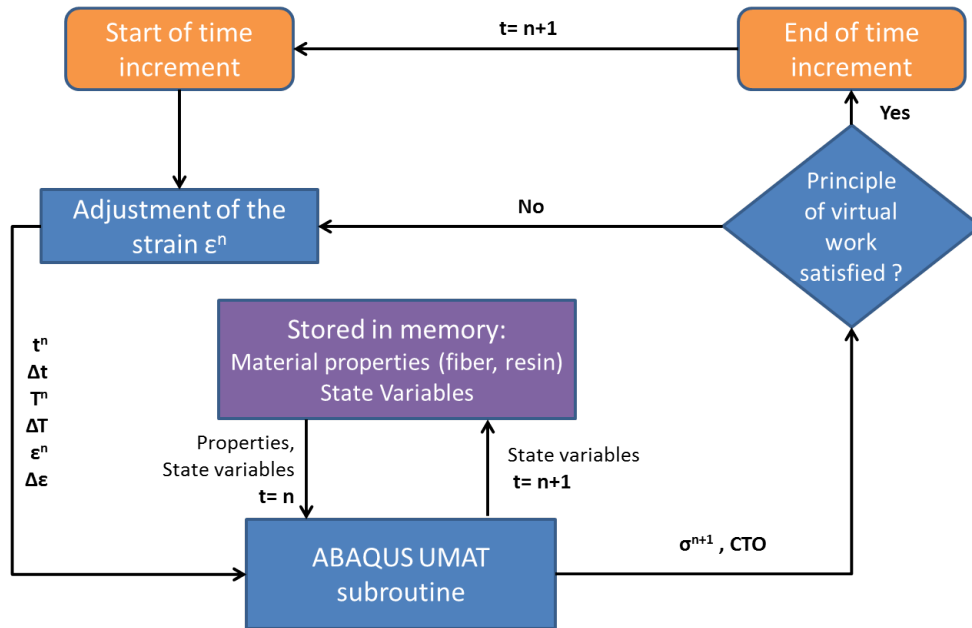


Figure B.4: UMAT solution process.



Figure B.5: The composite test frame studied.

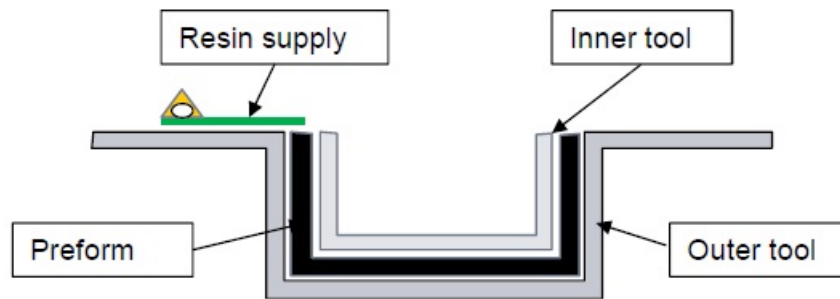


Figure B.6: Resin Infusion Process.

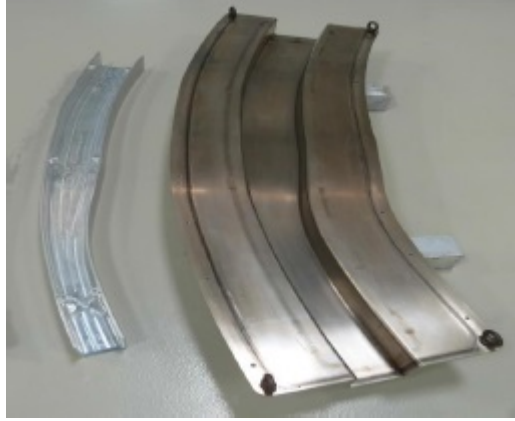


Figure B.7: The INVAR mould and the aluminium caul plate used.

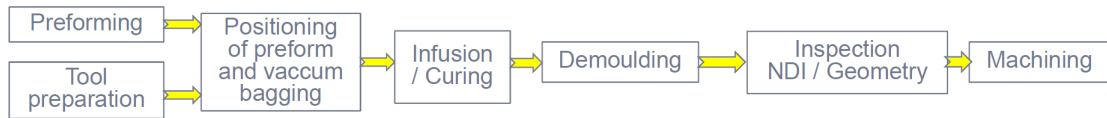


Figure B.8: The manufacturing process which was followed.



Figure B.9: The preform made from non crimp fabric.

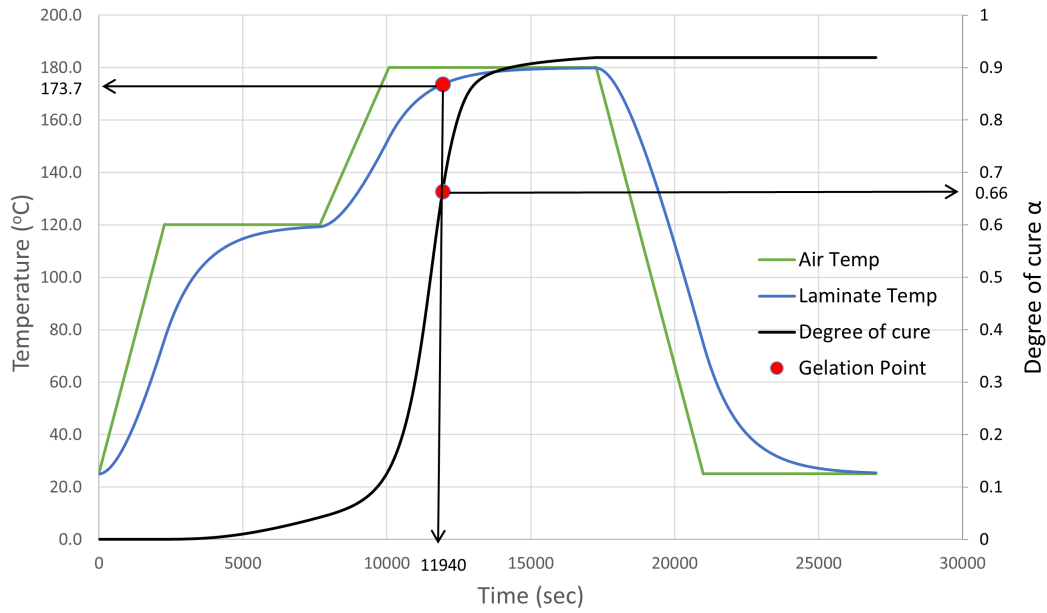


Figure B.10: The curing cycle used consisting of two dwells until 180°C is reached. The resulting laminate temperature is depicted with blue colour. The gelation point of the structure which is the starting point of the modelling effort is depicted as a red dot in the curing cycle as well as in the evolution of the degree of cure as predicted by Eq.(1).

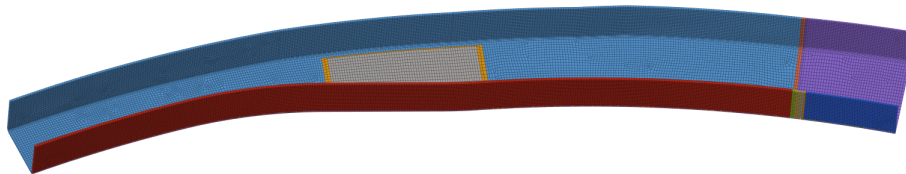


Figure B.11: The finite element mesh used to model the frame, consisting of 26433 C3D8I solid elements.

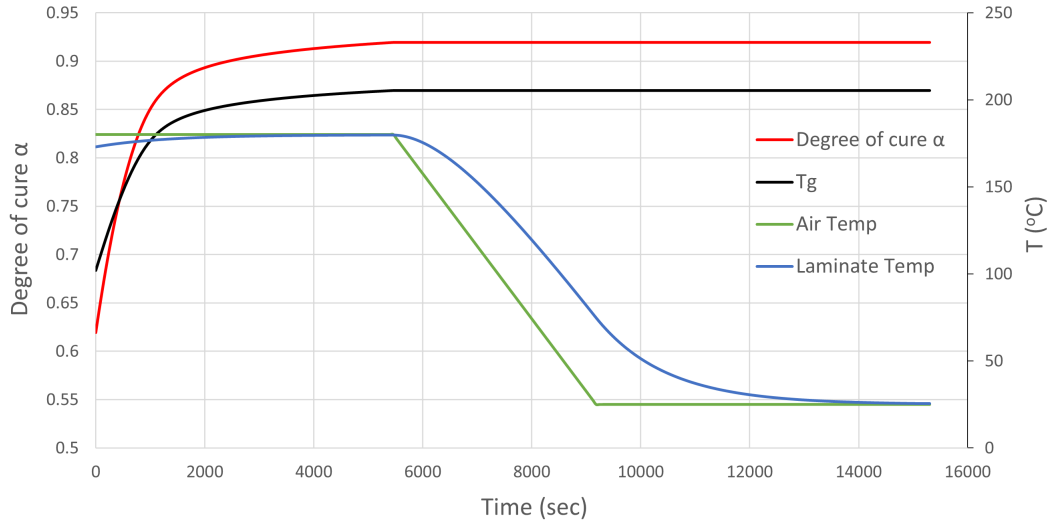


Figure B.12: The degree of cure α and the glass transition temperature T_g of the resin from the gelation to demoulding the structure.

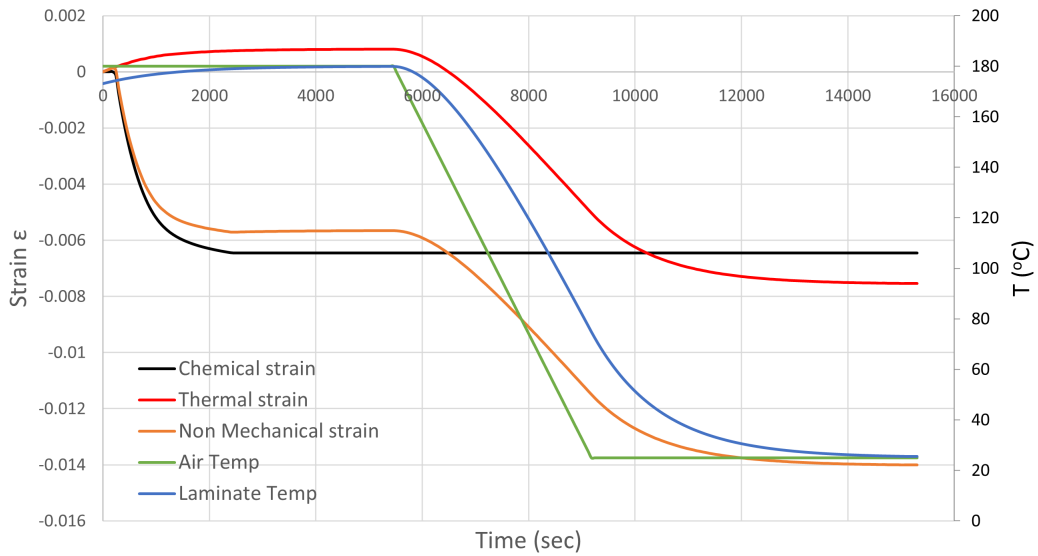


Figure B.13: Thermal and chemical strain of the resin from the gelation to demoulding the structure. The sum of the thermal and chemical strain equals at any point the non-mechanical strain.

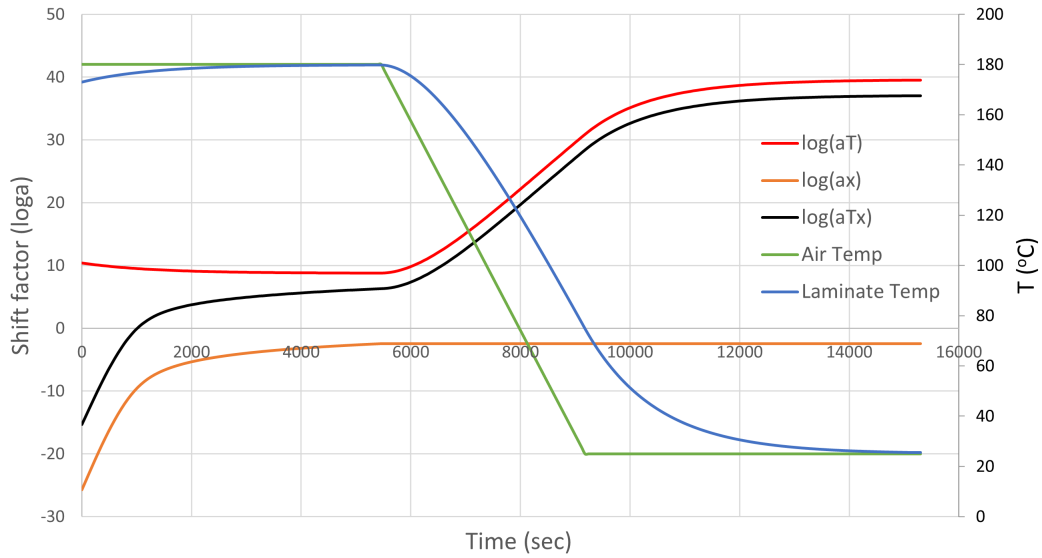


Figure B.14: The temperature, cure and the combined cure-temperature shift factor of the resin from the gelation to demoulding the structure.

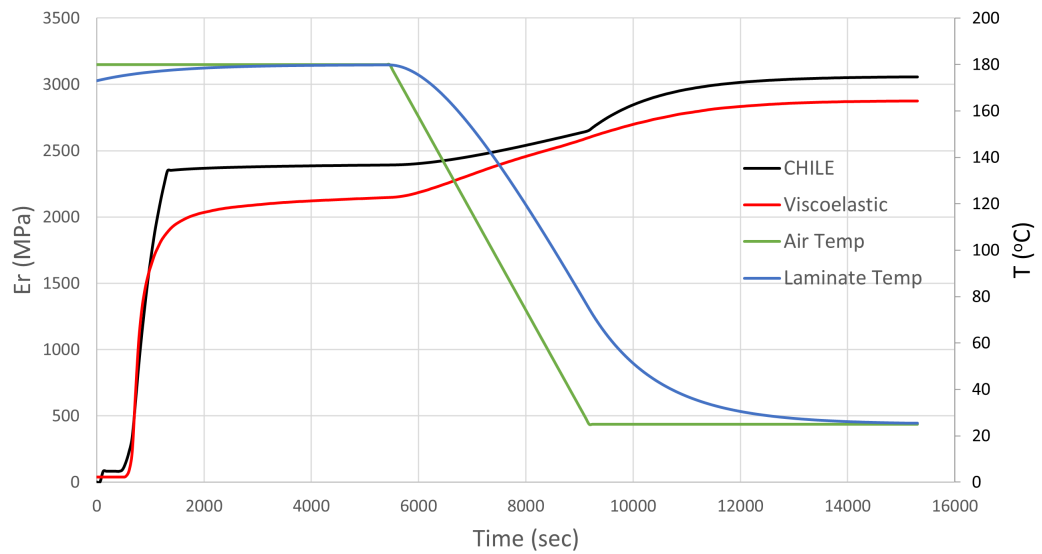


Figure B.15: The Young's modulus of the resin from the gelation to demoulding the structure, according to the CHILE and the viscoelastic material characterisation.

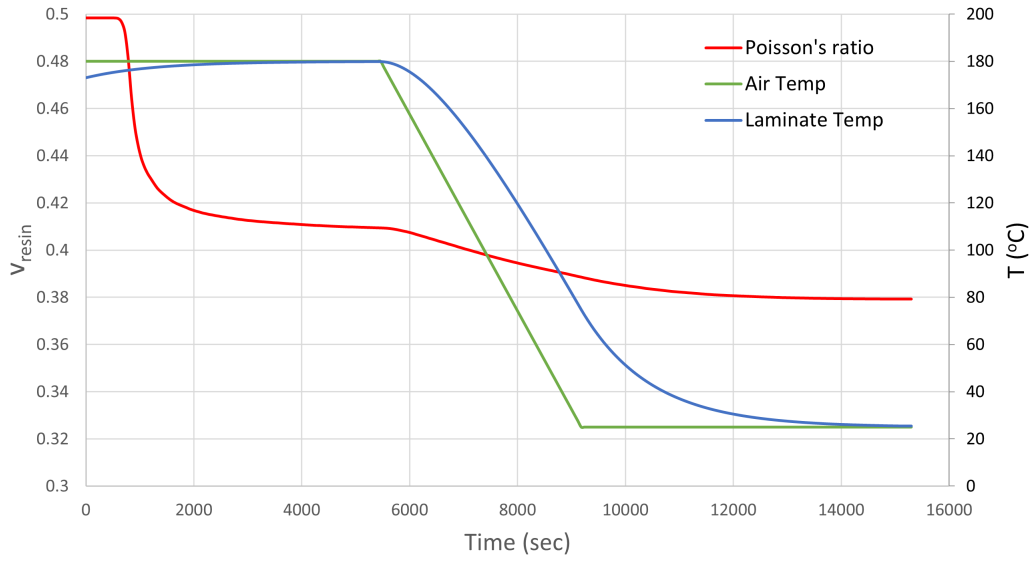


Figure B.16: Poisson's coefficient of the resin from the gelation to demoulding the structure.

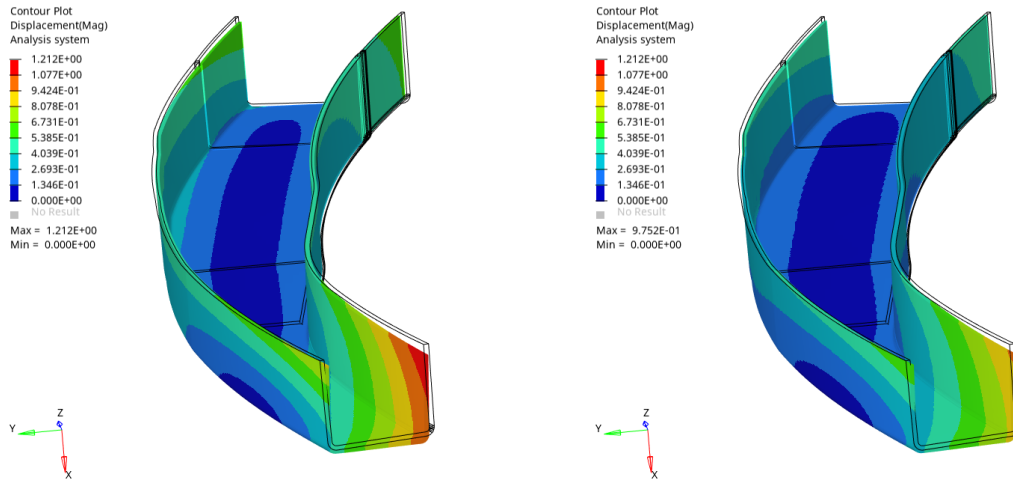


Figure B.17: Distortion fields after demoulding the frame (CHILE left, viscoelastic right).

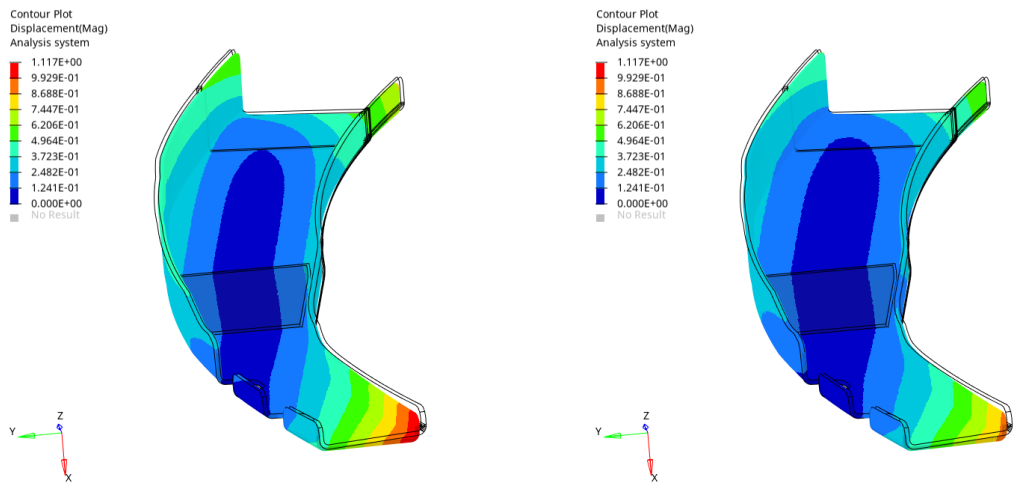


Figure B.18: Distortion fields after trimming the frame (CHILE left, viscoelastic right).

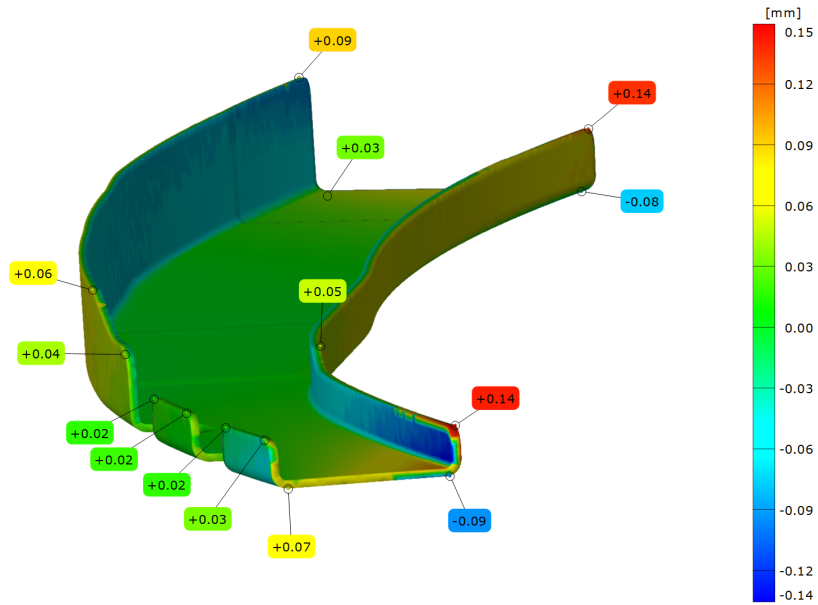


Figure B.19: The difference in the predicted distortion fields between the two material models.

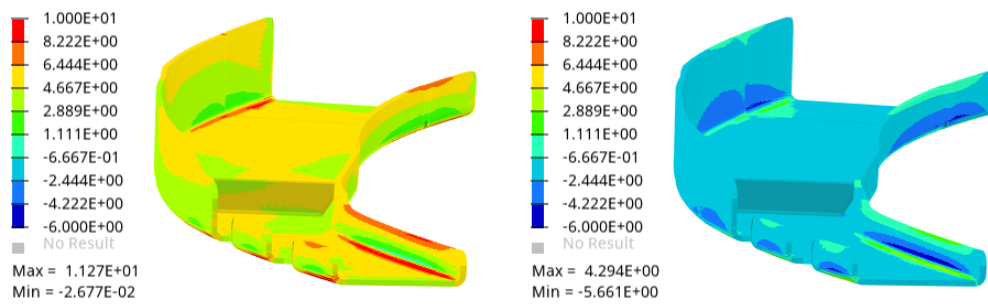


Figure B.20: The predicted residual stresses σ_{11} in the first layer (CHILE left, viscoelastic right).

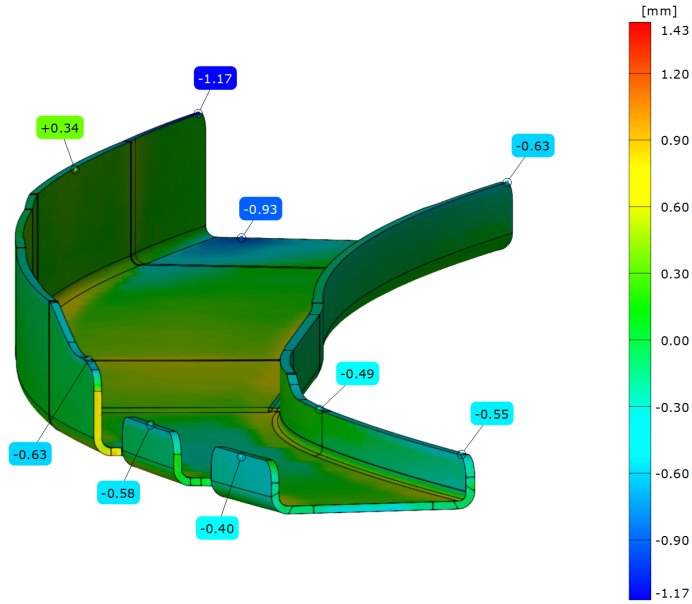


Figure B.21: Process induced distortion of the frame.

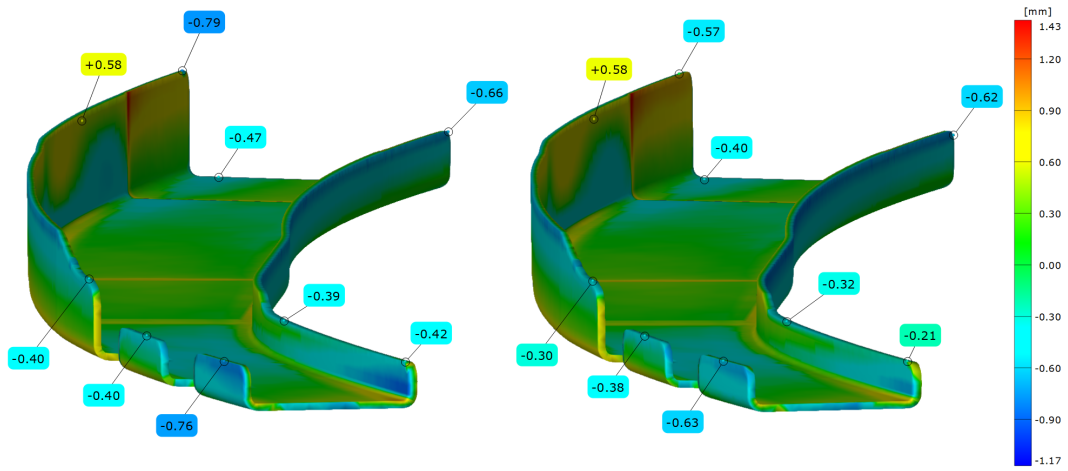


Figure B.22: Deviation between the measured distortions and the calculated ones (CHILE left, viscoelastic right).

Tables

Table B.1: Material properties of the IMS65 carbon fiber

Physical Property	Symbol	Value	Units	Source
CTE	CTE_{11}	-1.00 E-07	$[1/^\circ C]$	Approximated
	CTE_{22}	4.83 E-06	$[1/^\circ C]$	Approximated
E-Modulus	E_{11}	290	[GPa]	Toho Tenax [63]
	E_{22}	17.24	[GPa]	AS4 fiber [43]
	G_{12}	27.60	[GPa]	AS4 fiber [43]
Poisson's coef.	ν_{12}	0.20	-	AS4 fiber [43]
	ν_{23}	0.25	-	AS4 fiber [43]

Table B.2: Simulation steps

Step	Description	Temperature ($^\circ C$)	Degree of cure	Boundary Condition
1	Heating	180	$\alpha(T(t), \alpha_{t-1})$	Fixed
2	Hold	180	$\alpha(T(t), \alpha_{t-1})$	Fixed
3	Cool down	25	α_∞	Fixed
4	Demoulding	25	α_∞	Freestanding
5	Trimming	25	α_∞	Freestanding